Measuring river surface velocity using UAS-borne Doppler radar

Zhen Zhou[1], Laura Riis-Klinkvort[1], Emilie Ahrnkiel Jørgensen[1], Christine Lindenhoff[2], Monica Coppo Frías[1], Alexander Rietz Vesterhauge[2], Daniel Haugård Olesen[2], Makar Lavish[3], Alexey Dobrovolskiy[3], Alexey Kadek[3], Niksa Orlic[4], Tomislav Grubesa[4], Luka Drmić[4], Henrik Grosen[5], Sune Nielsen[5], Daniel Wennerberg[6], Viktor Fagerström[6], Jenny Axén[6], David Gustafsson[6], Peter Bauer-Gottwein[1]

[1]DTU Sustain, Technical University of Denmark, Kgs. Lyngby, Denmark
[2]DTU Space, Technical University of Denmark, Kgs. Lyngby, Denmark
[3]SPH Engineering, Riga, Latvia
[4]Geolux DOO, Samobor, Croatia
[5]Drone Systems Aps, Aarhus, Denmark
[6]SMHI Sveriges Meteorologiska och Hydrologiska Institut, Norrköping, Sweden

Corresponding author: Zhen Zhou (zhezh@dtu.dk)

Key Points:

- Unmanned Aerial Systems-borne Doppler radar can measure the river surface flow velocity
- We pick the correct river surface velocity from the raw Doppler spectra, using either a Gaussian one peak model, or a Gaussian two peak model
- The mean Particle Image Velocimetry results within the Doppler footprint verify the estimated velocities from Doppler radar

Abstract

Using Unmanned Aerial Systems (UAS) equipped with optical RGB cameras and Doppler radar, surface velocity can be efficiently measured at high spatial resolution. UAS-borne Doppler radar is particularly attractive because it is suitable for real-time velocity determination, because the measurement is contactless, and because it has fewer limitations than image velocimetry techniques. In this paper, five cross-sections (XSs) were surveyed within a 10 km stretch of Rönne Å in Sweden. Ground-truth surface velocity observations were retrieved with an electromagnetic velocity sensor (OTT MF Pro) along the XS at 1 m spacing. Videos from a UAS RGB camera were analyzed using both Particle Image Velocimetry (PIV) and Space-Time Image Velocimetry (STIV) techniques. Furthermore, we recorded full waveform signal data using a Doppler radar at multiple waypoints across the river. An algorithm fits two alternative models to the average amplitude curve to derive the correct river surface velocity: a Gaussian one peak model, or a Gaussian two peak model. Results indicate that river flow velocity and propwash velocity caused by the drone can be found in XS where the flow velocity is low, while the drone-induced propwash velocity can be neglected in fast and highly turbulent flows. To verify the river flow velocity derived from Doppler radar, a mean PIV value within the footprint of the Doppler radar at each waypoint was calculated. Finally, quantitative comparisons of OTT MF Pro data with STIV, mean PIV and Doppler radar revealed that UAS-borne Doppler radar could reliably measure the river surface velocity.

1 Introduction

With an increase in the frequency of extreme weather caused by global warming, high-resolution monitoring of rivers has become more important because floods are becoming more frequent and severe, and river maintenance and management are essential to adapt to these changes. In general, the focus of river monitoring is on the discharge parameter, which plays an important role in water resource planning and flood forecasting (Bechle et al., 2014; Yaseen et al., 2019; Fulton et al., 2020). To estimate river discharge, the cross-section averaged flow velocity (bulk velocity) is required. However, no contactless measurement techniques for bulk velocity currently exist and deployment of in-situ techniques such as Acoustic Doppler Current Profiler (ADCP) can be difficult or impossible during extreme flows and in remote and hard-to-reach areas. Contactless river discharge measurement techniques therefore often use river surface velocity as a

surrogate for bulk velocity and several methods exist to estimate bulk velocity from surface velocity (Alsdorf et al., 2007; Luce et al., 2013; Shi et al., 2019; Bandini et al., 2021; Bahmanpouri et al., 2022a; Bahmanpouri et al., 2022b). Therefore, it is urgent to develop more effective and efficient contactless river surface velocity monitoring technologies and to systematically assess the performance of such techniques against established in-situ monitoring technology such as electromagnetic flow sensors (e.g. OTT MF pro).

In recent years, non-invasive techniques have been developed to estimate river surface velocity. Optical image sequences acquired from helicopters or Unmanned Aerial Systems (UAS) platforms are processed using Particle Image Velocimetry (PIV) techniques to record instantaneous velocity fields (Fujita & Kunita, 2011; Detert & Weitbrecht, 2015; Tauro, Olivieri et al., 2016). PIV, which relies on tracking the displacement of patterns of particles in consecutive image frames, is the most widely used method to monitor the river surface velocity based on video sequences (Tauro et al., 2014; Tauro et al., 2016; Tauro et al., 2017). PIV results derived from UAS-borne videos in Danish and Swedish rivers indicated good agreement with OTT MF Pro results in the survey by Bandini et al. (2022), with errors of a few cm/s. A Parameter Optimization for PIV (POP) framework using helicopter-borne imagery was developed and employed in sediment-laden, large Alaskan rivers by Legleiter & Kinzel (2020). POP results obtained for a 200 m wide river indicated that this method was robust with a coefficient of determination (R^2) typically larger than 0.9. However, PIV has also some significant limitations, such as: 1) PIV results are vulnerable to the distribution of natural or artificial trackable features in the river; 2) PIV data processing workflows are time consuming and data volumes are large; 3) PIV requires good illumination (daylight conditions) and moderate wind. Another image-based technique, Space-Time Image Velocimetry (STIV), is a time-averaged velocity measurement method, which detects the main orientation of texture in a generated space-time image to obtain one-dimensional velocities on the water surface (Zhao et al., 2021). The technology was developed by Fujita et al. (2007), and the river surface velocity can be successfully measured by covering an area along the streamwise direction. In contrast to PIV with two-dimensional (2D) resolution, STIV is influenced not only by river seeding, illumination conditions, and wind but also generates results with a one-dimensional (1D) resolution along the search line direction.

The Doppler radar velocimetry method, as an entirely contactless, noninvasive technique, does not require seeding, daylight, and performance does not depend on river width. The method

is based on the Doppler effect and exploits the change in frequency of a radar signal reflected from the moving water surface to calculate the river flow velocity (Plant et al., 1990; Plant, 1997; Yurovsky et al., 2019). Plant et al. (2005) developed and tested a continuous wave (CW) Doppler microwave system (24 GHz), an airborne coherent real aperture radar (CORAR, 9.36 GHz), and a pulsed Doppler radar (10 GHz). The CW radar was mounted on a bridge and a cableway, while both pulsed Doppler radars were mounted on the riverbank and deployed from a helicopter and a light aircraft for CORAR. The stationary measurements were shown to be accurate to within ca. 10 cm/s when compared with in situ measurements. In the helicopter survey, when the helicopter was flown at low altitude, which increased the roughness of the water surface due to the propeller-generated downwash, the acquired velocity was consistent with ground-truth. Meanwhile, the light aircraft test was less successful. A portable, commercially available surface velocity radar (SVR) was applied by Welber et al. (2016). Results showed that the portable SVR-based discharge estimates were accurate within 10% for intermediate roughness flows, while larger errors were observed at very low relative roughness (< 0.05). Moreover, larger errors were found close to the riverbanks because of local disturbances of the flow such as secondary currents and eddies. UAVSAR, an L-band SAR technique was also used to measure the river surface velocity, results indicated that high velocity measurements correlated well with the river portions where high velocities are expected from river morphology (Biondi et al., 2020). Alimenti et al. (2020) developed a stationary prototype of a low-cost continuous wave (24 GHz) Doppler radar sensor and deployed it from a bridge in two sites along the Tiber River (Italy). Results were consistent with another reference radar and prior information of surface velocity distributions. Bandini et al. (2022) tested a static surface velocity radar (OTT SVR 100 from OTT HydroMet) from a bridge, holding the SVR static while pointing it both in the upstream and downstream direction in river Gudenå in Denmark. The results from the upstream-looking survey were better than from the downstream-looking survey, but both tests showed good agreement with in-situ measurements.

Although stationary and handheld radars proved able to monitor surface velocity with good consistency with the in-situ results (Fulton & Ostrowski, 2008; Welber et al., 2016; Lin et al., 2020), Doppler data from moving airborne platforms are still scarce and airborne deployment leads to several new challenges. The limiting factors such as the surface-scatterer quality, flight altitude and radar footprint, propwash, wind drift, and sample duration affect the quality of the reflected Doppler radar signals (Fulton et al., 2020). To date, only a few studies report actual UAS

deployment of a Doppler radar. Fulton et al. (2020) deployed a Doppler radar with 24 GHz continuous wave (CW) on the UAS platform in five flights over four different rivers in USA. Only the results for the location of maximum velocity were compared to handheld radar and acoustic Doppler velocimeter with differences within a few cm/s (ca. 1%). Furthermore, this study found that 15 cm/s is the minimum threshold of river surface velocity that can be successfully measured with the UAS-borne Doppler radar. Bandini et al. (2022) conducted surveys using the 24 GHz pulse UAS-borne Doppler radar (adapted from OTT SVR 100) over five rivers in Denmark and Sweden. Compared to in-situ velocimetry and PIV results, UAS-borne Doppler radar results were unreliable for rivers with too low water surface roughness; even for higher roughness rivers, poor repeatability illustrated the challenges of UAS-borne Doppler radar river velocimetry.

In this study, we employed a 24.125 GHz CW UAS-borne Doppler radar to measure five entire cross-sections (XSs) in Rönne Å in Sweden. Different from Bandini et al. (2022), we acquire the full waveform raw Doppler spectra with the new UAS Doppler radar payload. We propose an algorithm to pick the surface velocity from the Doppler spectra, fitting the average amplitude value of raw data from each waypoint across the river to a Gaussian one peak model, or a Gaussian two peak model (see Figure 1), separating the river surface velocity (called Doppler velocity) from the total velocity (the sum of the river surface velocity and the drone propwash induced velocity) when relevant. For each XS, different flight altitudes (1.5 m, 2.1 m, 4.1 m, 5.1 m, and 6.1 m) were tested to understand the impact of variable footprint size and propwash intensity on the quality of the Doppler data. UAS-borne RGB videos were processed with both PIV and STIV. Overlaying the Doppler radar footprint on the PIV results, we can compare the surface velocity derived from radar to the PIV velocities observed within the footprint. An electromagnetic current meter (OTT MF Pro) (Egg et al., 2017; Mutzner et al., 2019; Randklev et al., 2019) was used for in-situ measurements along the XS at 1 m spacing. Finally, three different surface velocities (radar, mean PIV and STIV) derived from the UAS platform are compared with the OTT MF Pro values. Results indicate that UAS-borne Doppler radar can provide reliable river surface velocity in the five surveyed XSs.

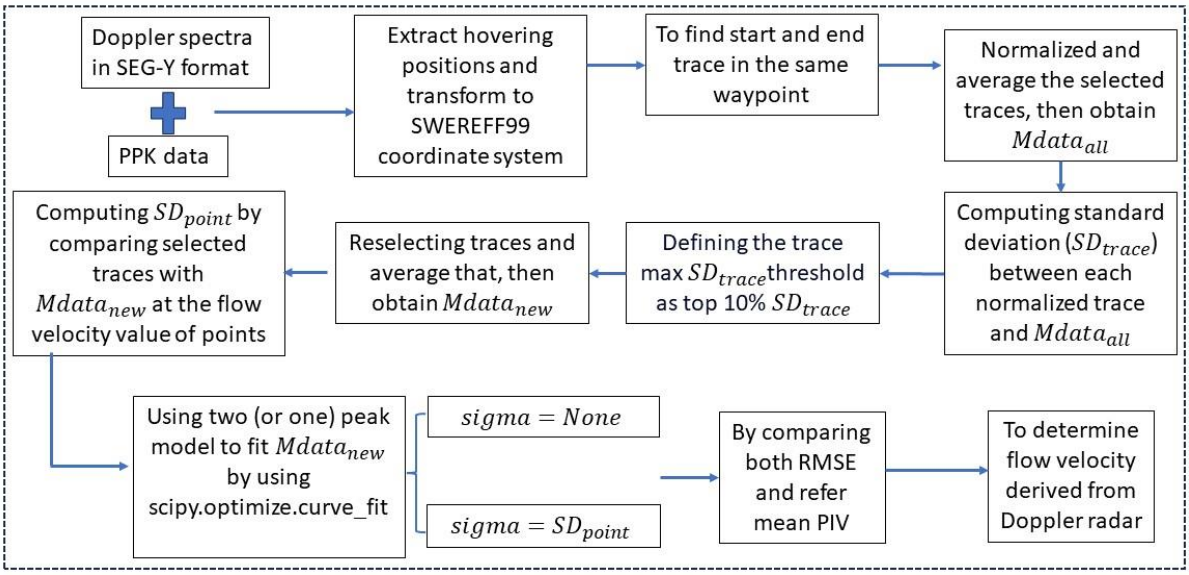

Figure 1. Proposed workflow for searching the optimized traces number at one waypoint and two fitting appoaches by using (or not using) $sigma$ in the fitting function.

2 Materials and Methods

2.1 Radar velocimetry based on Doppler shift

In Doppler radar velocimetry, we measure the difference between the frequency of transmitted and reflected microwave signals when the emitted wave encounters a moving object relative to the transmitter. The frequency shift becomes positive or negative depending on whether the object is moving towards or away from the radar (Chan & Jardine, 1990; Fulton & Ostrowski, 2008; Shames et al., 2013). The radar-recorded frequency shift can be translated into the radial velocity of the observed object. When the radar is used to measure rivers, the line-of-sight surface velocity relative to the radar itself can be obtained from the frequency shift. A simplified overview of the Doppler shift is shown in Figure 2a. The observed shift in frequency will depend on the radial velocity of the target as shown in equation (1):

$$\Delta f = \frac{2u_r f_0}{c}, \quad (1)$$

where Δf is the Doppler shift frequency, u_r is the velocity of moving object relative to the radar source, c is the velocity of the transmitted signal (speed of light) and f_0 represents the center frequency of the Doppler radar. In this paper, the center frequency f_0 is 24.125 GHz. The incidence angle of the transmitted radar signal on the water surface was 45 degrees in this study. Therefore, the river surface velocity can be obtained from equation (2):

$$u_r = \frac{\Delta f c}{2 f_0 \cos(45^\circ)}. \quad (2)$$

Because of the oblique incidence of the transmitted microwaves, some degree of surface roughness is needed to ensure sufficient backscatter in the direction of the transmitter. Typically, when the free surface of the water is too smooth, the specular reflection of the radar beam dominates over Bragg scattering (Fulton & Ostrowski, 2008; Welber et al., 2016), which leads to weak backscatter signals and unreliable velocimetry results.

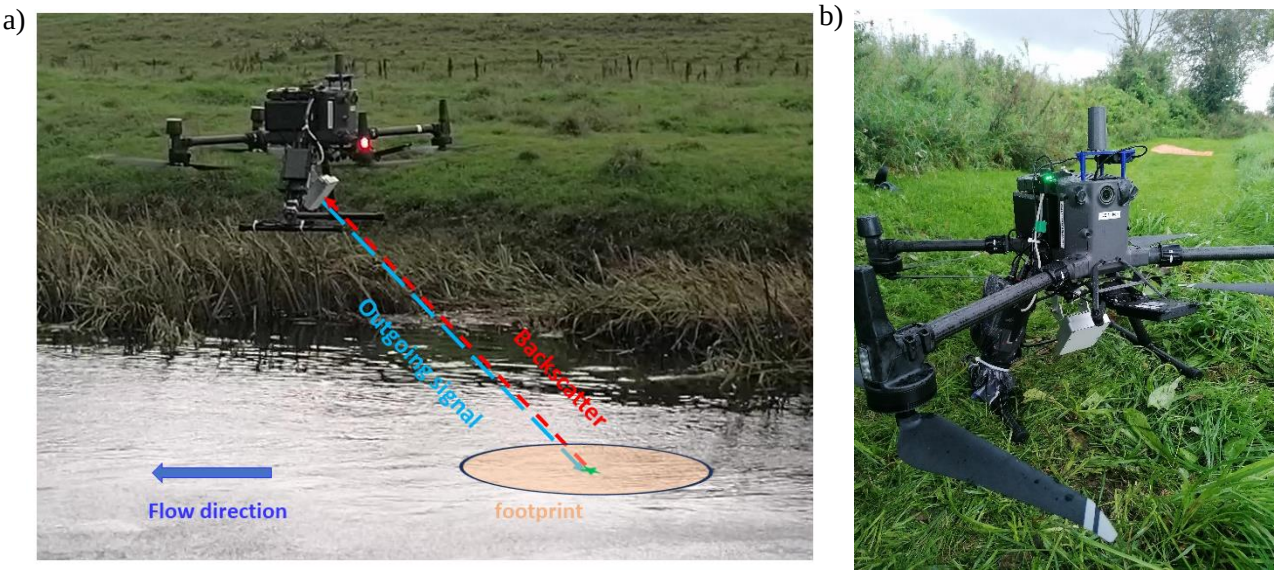

Figure 2. a) Describes the measuring process of a drone with Doppler radar located in one waypoint. Doppler radar always looks against river flow direction, and considering the incidence angle (45 degrees), the radar can receive the backscatter energy located in the ellipse area named footprint. b) Shows the DJI Matrice 300 RTK carrying Geolux RSS-2-300W Doppler radar, in which the radar is the white square mounted below the main body of the drone.

2.2 Doppler radar deployment and interpretation of Doppler spectra

In the present study, we tested the Geolux RSS-2-300W Doppler radar onboard a DJI Matrice 300 RTK (Figure 2b). During the planned flight, the UAS equipped with the Doppler radar was hovering at each waypoint to retrieve observations for measurement periods of about 1 min. The flight direction between two waypoints was planned to keep the UAS nose pointing perpendicular to the river flow. During the radar measurements, the radar was always looking against the flow direction. The Doppler radar is a continuous wave (CW) radar with a K-band frequency at 24.125 GHz, which lies in the microwave spectrum. The radar emits microwaves with

a wavelength of 12.5 mm when traveling in the air. The radar works for river velocities between 0.02 m/s to 15 m/s with a velocity resolution of 7.3242 mm/s. The sampling rate is 10 sps (samples per second) and measurement repeatability error is <1% of the true measured value. The Doppler radar used in this study is an experimental modification of Geolux RSS-2-300 adapted for airborne deployment and providing access to the raw Doppler spectra output.

The UAS is equipped with a GNSS RTK (Real-Time Kinematic) receiver compatible with GPS, GLONASS, BeiDOU, and Galileo systems. According to DJI (www.dji.com) this quadcopter typically has a hovering accuracy of ± 0.1 m (in low-wind conditions) horizontally and vertically in D-RTK mode. The RTK positioning accuracy is reported to be 1 cm + 1 ppm horizontally and 1.5 cm + 1 ppm vertically. In the field, the drone RTK was sometimes temporarily offline due to failure of mobile data connection. During such periods, Post-Processed Kinematics (PPK) was used to obtain accurate positions of the drone. PPK works similar to RTK, but does not rely on having a real-time datalink. PPK uses GNSS observations stored in Rinex format from the rover (on the UAS) and from a fixed base station (Lacambre et al., 2022). PPK processing was carried out using the freeware Emlid Studio 1.6 (Eker et al., 2022; Tamimi & Toth, 2023). In order to obtain high absolute accuracy, it is necessary to obtain the raw GNSS observation from the base station and the drone as well as accurate coordinates of the base station provided by either RTK or Precise Point Positioning (PPP, Ge et al., 2008).

The Doppler radar outputs the raw Doppler data, i.e. return power of 4096 frequency bins at a trace rate of 10 Hz. The raw data is stored in SEG-Y format (Siegert et al., 2017). In fact, it is difficult to find the correct river surface flow velocity from the raw data because of two reasons. First, a broadening of each of the peaks in the spectrum usually occurs due to different reflections within the footprint (other scattering mechanisms than Bragg scattering) and a variation in the local incidence angle; secondly, the intensity of the peaks can vary (Plant et al., 2005) and it is not always straightforward to identify the peak corresponding to the true surface velocity.

The obtained Doppler spectra are an average of the samples recorded during the hovering period at each waypoint. Therefore, drone velocity is negligible and surface scattering will primarily be caused by larger waves representing the river surface velocity. The one-minute hovering interval was chosen to average out other influence factors such as rain drops or eddies. Considering that only one primary flow direction exists in a river, the assumption is that the

Doppler spectra would have one peak representing the river surface velocity. In fact, a second peak is visible in most of the recorded Doppler spectra due to the drone causing propeller-induced water movement on the water surface (called propwash in this study). The propwash velocity is assumed to be isotropic and directed in the radial direction. Under these assumptions, we would expect to see peaks at the following two velocities in the raw Doppler spectra:

$$V_{peak1} = -V_{river}, \tag{3}$$

$$V_{peak2} = V_{propwash} - V_{river}, \tag{4}$$

where we assume that the radar points in the upstream direction, which is defined as the positive direction. River flow velocity is thus in the negative coordinate direction, while propwash velocity in the pointing direction is positive.

2.3 Doppler radar footprint analysis

The return signal received by the Doppler radar represents an average over the beam area on the river water surface, also referred to as an illuminated area or footprint. The beam size is an ellipse, projected onto the ground, the area of which depends on the horizontal beam width and the distance between the antenna and the target. Moreover, the radar has a tilt angle with respect to horizontal, denoted by θ. Here the RSS-2-300W Doppler radar has beam angles of 12 degrees in azimuth direction (horizontal), denoted by θ_a, and 24 degrees in elevation (vertical direction), denoted by θ_r. Figures 3a and 3b show the beam and the footprint areas, where the blue ellipse depicts the beam, and the red ellipse is the footprint.

To calculate the exact area of the footprint, it is necessary to determine the major and minor axis of the footprint described in equations (5) and (11), and we set $\alpha = 90^{\circ} - \theta$:

$$a = \frac{1}{2}\left[H \cdot \tan\left(\alpha + \frac{\theta_r}{2}\right) - H \cdot \tan\left(\alpha - \frac{\theta_r}{2}\right)\right], \tag{5}$$

where H is the altitude of the drone. θ And θ_r are the tilt angle and the beam angle in vertical direction (elevation angle), respectively.

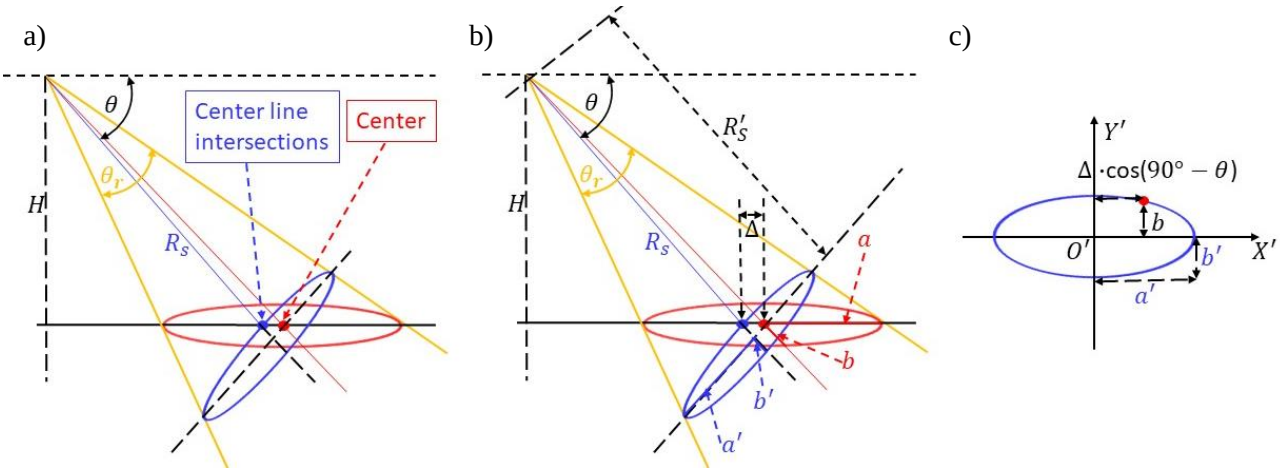

Figure 3. Visualizations of different steps to derive the footprint size of the drone with Doppler radar. In a), the red ellipse is the ground projection, the blue is the beam size, and H is the altitude of the drone. The blue point is the center line intersection with the blue ellipse and the red point is the center of the projected footprint. θ And θ_r represent the tilt angle and the elevation angle, separately. In b), the footprint ellipse consists of the major axis a and the minor axis b. In addition, the beam area is drawn by a blue ellipse with the major axis a' and the minor axis b'. And Δ is the difference between the centerline intersection of the beam and the center of the footprint. R_s and R_s' represent the slant range from the drone to the river surface and the centerline intersection of the beam, separately. c) Shows the beam area described with the $X'O'Y'$-coordinate system, the selected point marked as a red point with coordinate value $X' = \Delta \cdot (\cos(90° - \theta)), Y' = b$.

From Figure 3b it is shown that there is a difference between the centerline intersection of the beam (the blue ellipse) and the center point of the projected footprint (red ellipse), which is denoted by Δ. This can be found as:

$$\Delta = a - H.\left[\tan(\alpha) - \tan\left(\alpha - \frac{\theta_r}{2}\right)\right]. \quad (6)$$

Next, the parameter R_S' in Figure 3b can be expressed as:

$$R_s' = R_s + \Delta \cdot sin\alpha, \quad (7)$$

where R_s is the slant range from the source to the extent of the off-nadir angle α, hence, given as:

$$R_s = \frac{H}{cos\alpha}. \quad (8)$$

Further, the footprint semi-major and semi-minor axis (called a' and b') are found in the blue ellipse in the $X'O'Y'$-coordinate system (see in Figure 3c) through equation (9):

$$\begin{cases} a' = R_s' \cdot \tan\left(\frac{\theta_r}{2}\right), \\ b' = R_s' \cdot \tan\left(\frac{\theta_a}{2}\right). \end{cases} \quad (9)$$

Considering the elliptical equation in the $X'O'Y'$-coordinate system with the centre being the midpoint of the beam footprint (blue ellipse) in point $O' = (0, 0)$, and selecting the point of $X' = \Delta \cdot (cos\alpha), Y' = b$, we obtain the following equation:

$$\frac{(\Delta \cdot cos\alpha)^2}{(a')^2} + \frac{b^2}{(b')^2} = 1, \quad (10)$$

and solving equation (10) for the semi-minor axis:

$$b = \frac{b'}{a'} \cdot \sqrt{(a')^2 - [\Delta \cdot (cos\alpha)]^2}\,. \quad (11)$$

The distance from nadir of the radar to the center of the projected footprint onto the water surface (red ellipse in Figures 3a and 3b), is called the ground range (GR), can be found as:

$$GR = H \cdot \tan\alpha + \Delta, \quad (12)$$

the GR parameter can be used to plan the flight path of the Doppler radar to ensure that footprints are centred on points of interest, for instance points where the surface velocity was measured in-situ.

2.4 Fitting Doppler signals with Gaussian models

2.4.1 Doppler data processing steps

We extract drone positions from PPK flight positioning logs, reference them to a cross section coordinate and convert them to the horizontal coordinate reference system (CRS) SWEREF 99 TM (Kempe et al., 2016); We use the SWEN17 RH2000 geoid model (Swedish-geoid-models) for Sweden as the vertical reference. The cross-section coordinate is increasing along the cross-section from the left bank to the right bank. It is zero at the intersection with the river centerline. Subsequently, traces belonging to each waypoint were extracted from the raw Doppler data in SEG-Y format. Drone position (expressed as cross-section coordinate) was plotted against the trace number for each flight (Figure 4a) and waypoints were identified as periods of stable drone position separated by periods of rapid drone movement. Start and stop trace numbers for each waypoint were graphically extracted and the corresponding traces were saved in separate Doppler spectra for each waypoint (Figure 4a).

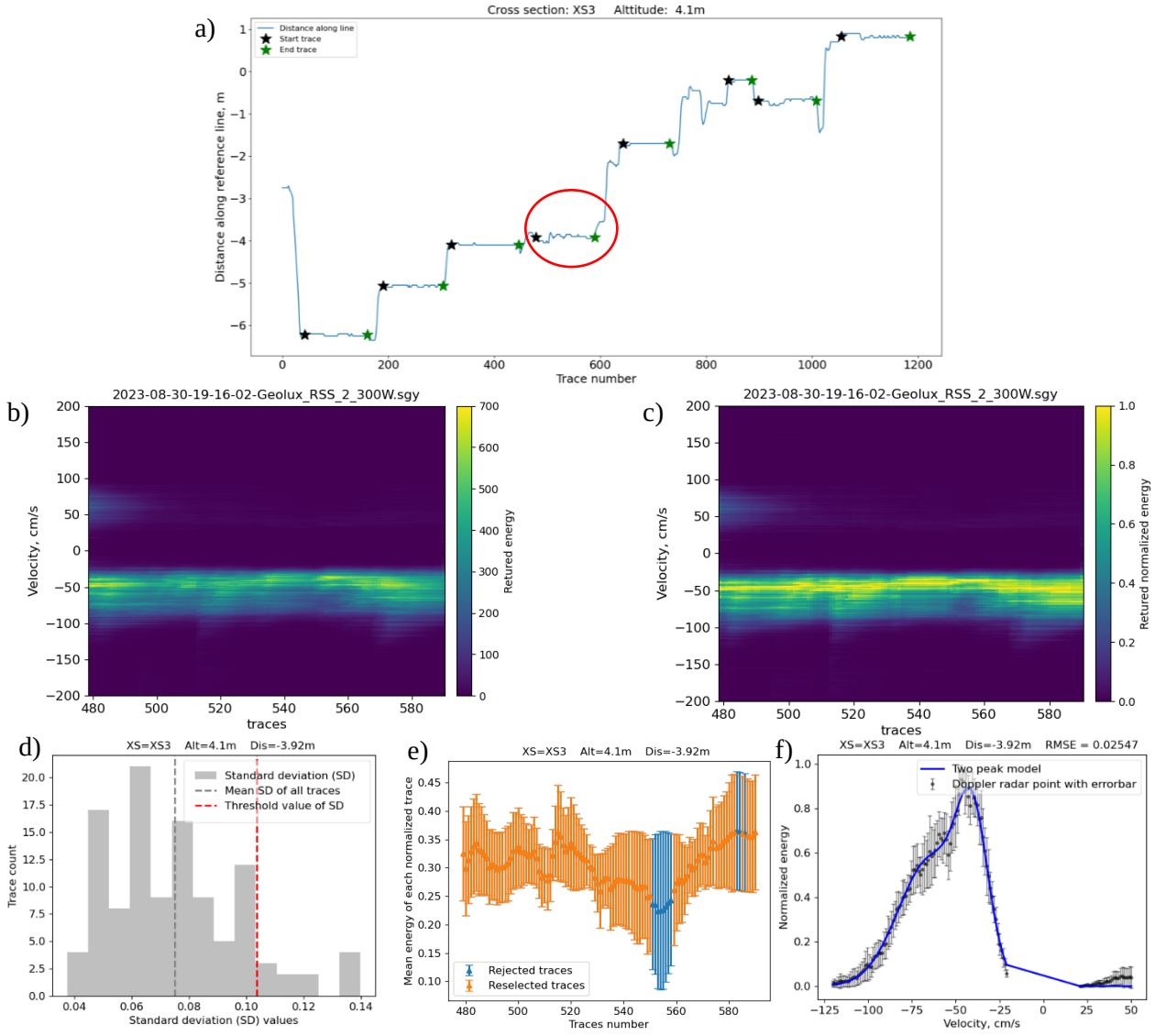

Figure 4. a) Using XS3 as an example to show how to find the start and end trace in one waypoint. b) And c) show full waveform plots of the signal and the normalized signal energy based on the maximum of each trace at the same waypoint (indicated by the red circle in Figrue 4a), respectively. In d), the distribution of standard deviation (SD_{trace}) between each trace and the Doppler normalized amplitude averaged over selected traces ($Mdata_{all}$) at the waypoint (distance= -3.92 m). The vertical dashed red and grey lines indicate the selected max SD_{trace} threshold and a mean SD_{trace} value. e) A comparison between reselected traces and rejected traces with SD_{trace} error bar. In f), black points indicate the normalized amplitude averaged over reselected traces ($Mdata_{new}$). The error bars represent the standard deviation (SD_{point}) of comparing selected traces with $Mdata_{new}$ at the flow velocity value point by point. A Gaussian two peak model shown by the blue line was applied to fit $Mdata_{new}$. Note that all results are calculated by using the normalized traces from Figures 4d to 4f.

Figure 4b shows a Doppler spectrum for one selected waypoint. Return power may be variable across traces, for instance, due to slight changes in the beam incidence angle resulting from drone vibrations. To even out such power variations, each trace was normalized by the maximum return power occurring in this trace. The result is shown in Figure 4c. Moreover, we average the amplitude energy of all selected traces for the same waypoint and frequency bin and obtain the mean amplitude as a function of frequency for each waypoint ($Mdata_{all}$). Afterwards, the standard deviation (SD_{trace}) between each normalized trace and $Mdata_{all}$ is calculated, and traces with high SD_{trace} values are rejected. Here we set the max SD_{trace} threshold (red vertical dashed line in Figure 4d) as the top 10% values for most waypoints, which means the mean value of reselected traces $Mdata_{new}$ does not include the top 10% traces (blue traces in Figure 4e). The standard deviation (SD_{point}) of each frequency bin across the reselected traces is also calculated to provide a measure of the confidence of each frequency bin in the $Mdata_{new}$ dataset (Figure 4f).

2.4.2 Fitting Doppler signals with one peak Gaussian model

For higher river surface velocities (i.e., surface velocity > 80 cm/s), the drone-induced propwash velocity can be ignored because propwash is pushed downstream by the flow and does not significantly influence the flow field at the location of the Doppler footprint. Therefore, a Gaussian one peak model is used to fit $Mdata_{new}$ by weighted least-squares fitting 'scipy.optimize.curve_fit' in Python (scipy.optimize.curve_fit). Equation (13) describes the return energy predicted by the one peak model:

$$A(x) = f exp\left(-\left[\frac{x-\mu}{\sigma}\right]^2\right), \quad (13)$$

where A is the return energy (amplitude of the Doppler spectrum). μ, σ, and f are the mean, the standard deviation, and the weight parameter, respectively, which are estimated by the fitting function and x is the velocity.

2.4.3 Fitting Doppler signals with two peak Gaussian model

When the Doppler radar measured in the river's lower flow velocity portions (i.e., surface velocity between 30 cm/s and 80 cm/s), the river surface velocity and drone-included propwash velocity should be found in Doppler data, therefore the model based upon a Gaussian double peaks' distribution is applied. The two peak model can be generated by adding two Gaussian one peak distributions. The amplitude as a function of velocity is predicted as (14):

$$A(x) = f_1 exp\left(-\left[\frac{x-\mu_1}{\sigma_1}\right]^2\right) + f_2 exp\left(-\left[\frac{x-\mu_2}{\sigma_2}\right]^2\right), \quad (14)$$

where μ_1 and μ_2 are the means of two Gaussian distributions, while σ_1 and σ_2 are the standard deviation values, f_1 and f_2 are the weight parameters. The two means, which are estimated by the fitting algorithm, represent the two peak velocities (equations 3 and 4).

As indicated in Figure 1, to find suitable final Gaussian models by fitting one or two Gaussian peak model with starting parameters and $Mdata_{new}$, we set two scenarios in the weighted least-squares fitting process by using $sigma = SD_{point}$ and $sigma = None$ (scipy.optimize.curve_fit). Then, comparing both RMSE values between modelled results and $Mdata_{new}$, and referring mean PIV within the footprint for two scenarios, we choose the solution with a smaller RMSE value and closer to the mean PIV. In these solved parameters, μ in the Gaussian one peak model represents Doppler velocity; μ_1 and μ_2 in the Gaussian two peak model represent the Doppler velocity and the total velocity. In Figure 4f, black points represent $Mdata_{new}$, and error bars mean SD_{point} ($sigma = SD_{point}$), and we solve the modelled results (blue line) by using the fitting function with $sigma$.

2.5 Complementary Measurements

Simultaneous velocity measurements were carried out using an OTT MF Pro instrument (OTT HydroMet, Kempten, Germany). The OTT MF Pro is used to measure the river surface velocity along the cross-section. In the measurement process, the sensor head of OTT MF Pro needs to be fully submerged in the flow, so observations could not be acquired exactly at the surface level but a few centimeters below the water surface (De Schoutheete et al., 2019; Bandini et al., 2021). In this study, the measurements were carried out every 1 m from one side of the river to the other and a Fixed Period Average velocity with a default period of 30 seconds was applied.

In addition, UAS-borne RGB videos were recorded for all cross sections. Videos of the river flow at each cross-section were taken using a Phantom 4 Pro by DJI (Taddia et al., 2019) and a video-camera GoPro Hero 5 in 1080p HD with 60 frames per second (Zoltie & Ho, 2018). For post-processing the videos, we use Particle Image Velocimetry (PIV) and STIV techniques (Fujita et al., 2007; Bandini et al., 2022).

PIV tracks patterns on the surface to obtain the flow field using similarity and pattern recognition algorithms (Westerweel, 1995; Hain, & Kähler, 2007; Strelnikova et al., 2020). In general, visible seeding on the surface and sufficient daylight are necessary (Bandini et al., 2021). Here we use the OpenPIV package in Python to obtain surface velocity estimates. From each video, we extract frame pairs (pair separation 5 frames), spaced in time by 50 frames and process each frame pair individually. We reject outliers falling outside reasonable upper and lower velocity limits, chosen individually for each cross section. In addtion, by using two ground control points (GCPs) in the image with known real world coordinates (see red triangles in Figure 6), we estimate the spatial scale as the ratio of the real-world distance between GCPs and the image distance in pixels. Finally, the flow velocity is calculated as the vector sum of the velocities in both image directions, as indicated in equation (15):

$$V_{PIV} = \sqrt{v^2 + u^2}. \tag{15}$$

The second video velocimetry approach used here is Space-Time Image Velocimetry (STIV), which is a time-averaged velocity measurement technique and uses the UAS-borne videos to detect the Main Orientation of Texture (MOT) in a generated Space-Time Image (STI) to obtain one-dimensional velocities on the water surface (Zhao et al., 2021). Based on video images acquired from UAS-camera, STIV is applied to river surface velocity measurements with search lines parallel to the river flow direction. Usually, search lines with a constant length in the physical scale are set at a constant spacing in ortho-rectified images (Fujita et al., 2019). Search lines setting, covered widths, and STIV results of five XSs can be found in Table 1.

Table 1. *Overview of search line setting and STIV measument results for five XSs at Rönne Å.*

Cross-sections	*Search lines length (m)*	*Search lines spacing (m)*	*Covered width (m)*	*STIV average velocity (cm/s)*	*STIV max velocity (cm/s)*
XS1	15.0	0.644	12.226	33.9	52.1
XS2	3.0	0.77	14.627	94.7	144.1
XS3	3.0	0.439	8.343	55.6	80.1
XS5	7.0	0.704	13.382	29.8	55.8
XS6	10.0	0.646	12.278	44.1	71.0

3 Study Sites

Field data were collected from 29th of August to 31st of August 2023 at Rönne Å in South Sweden (Figure 5). Five XSs are selected, and cross-section taglines are established to mark the cross-sections in the field. The tagline is set up perpendicular to the flow direction. The right and

left banks are determined by convention as right and left looking in the downstream direction. All days except 31st of August 2023 had mild weather conditions with dominant sunshine and light wind. On 31st of August 2023, strong rainfall occurred during the Doppler measurement in XS5. River water levels were high with some flooding of the surrounding fields for some stretches after a longer wet period prior to the survey. Table 2 shows an overview of the field coordinates, the survey dates, the average depth, the stream width, and the aquatic vegetation distribution. Aerial photos of the five XSs can be found in Figure 6, where the exact locations of Doppler radar measurement waypoints with different altitudes are shown as solid circles. Videos of the flow at the XSs are included in the online data repository, along with all other raw and processed datasets (Roenne Aa Survey, Sweden). In addtion, Figure 6 also shows the exact positions of the in-situ surface velocity measurements using OTT MF Pro, which are indicated with pink points along taglines. It is noted that XS2 has a much lower depth and faster flow velocity than other cross-sections, and that in XS5, a Matrice 300 drone was flying close to the left bank during the PIV video acquisition, causing significant disturbances of the surface velocity field due to propwash.

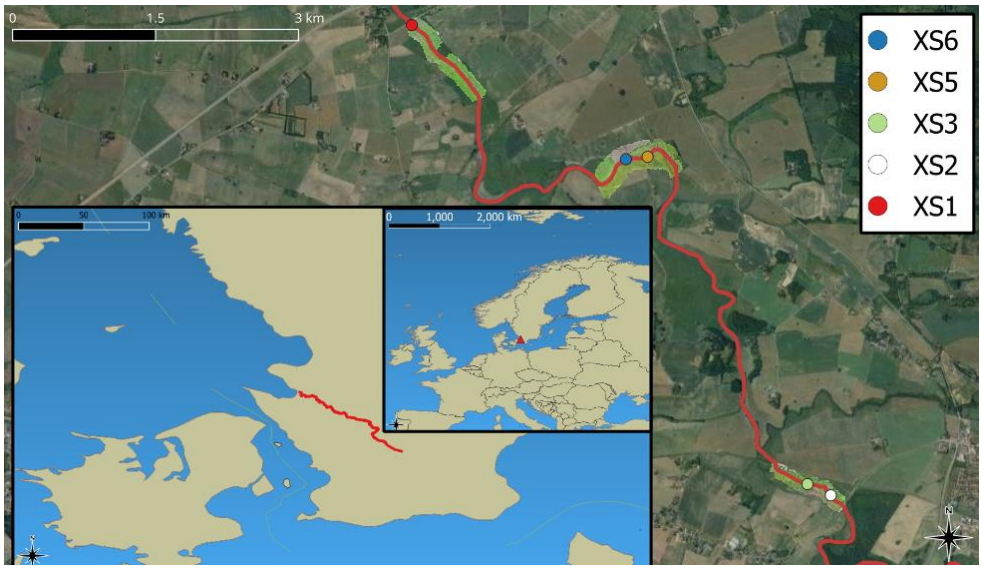

Figure 5. The inserted overview map shows the measured river location of Rönne Å in Sweden (red triangle and line) (source for the inset map is from natural earth data). Selected five cross-sections measured by drone with RSS-2-300W Doppler radar are shown using solid circles. Red line indicates the river survey centerline.

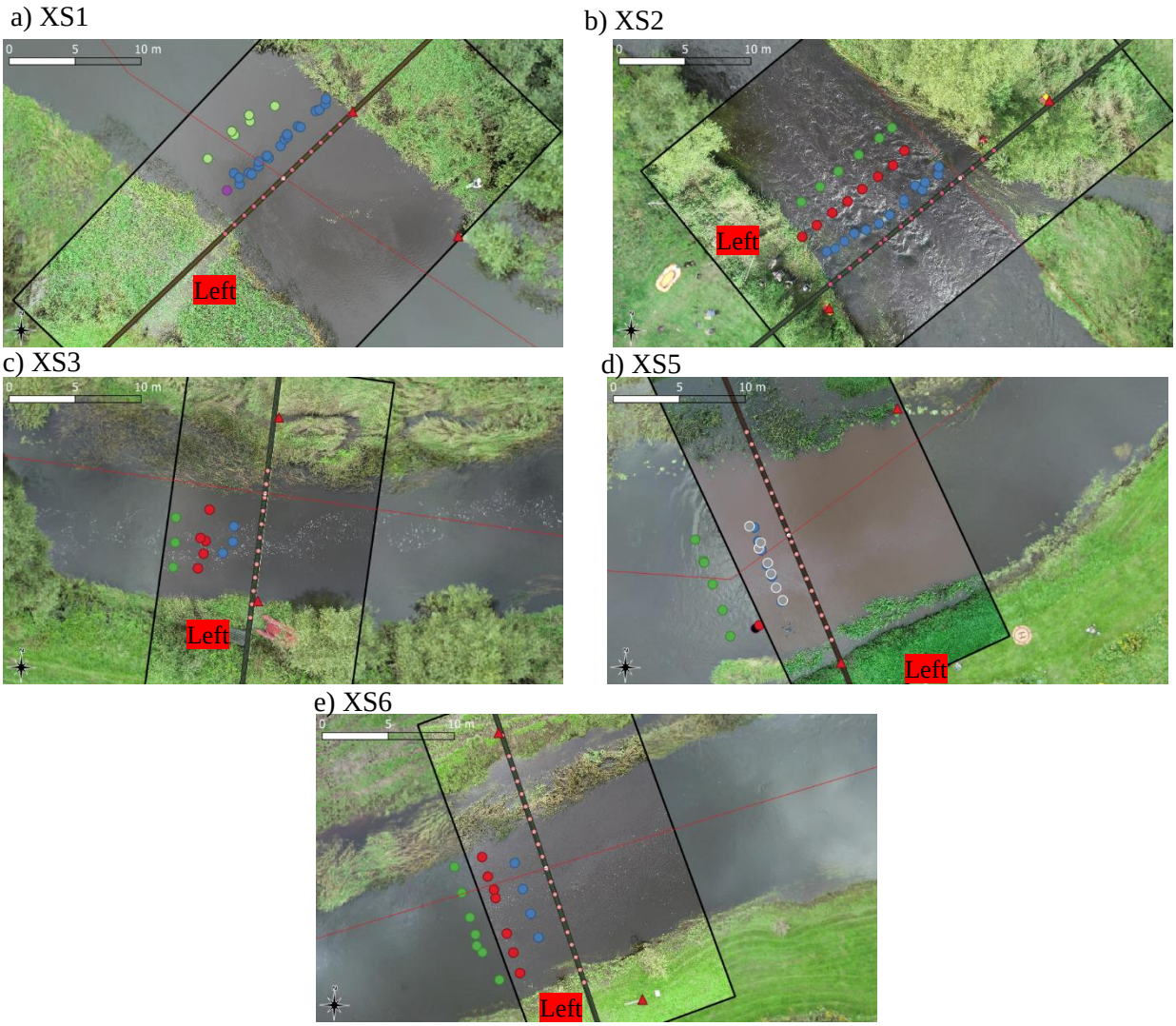

Figure 6. Shows drone positions with different fly altitudes by using RSS-2-300W Doppler radar for measuring river surface velocity. Solid circles present different drone waypoints, in which magenta, blue, red, lime, and green represent the drone fly altitudes with 1.5 m, 2.1 m, 4.1 m, 5.1 m, and 6.1 m, respectively. In addtion, pink points along with taglines express the measured positions by using OTT MF Pro, and the white point is the tagline zero-point of each cross-section. Red triangles are selected reference points, which are used to determine the transformation relation between pixel coordinates and geographical coordinates. Red line is the survey centerline. Note that grey and black soild circles in Figure 6d indicate the drone waypoints with 2.1 m and 4.1 m altitudes before rain, the other waypoints are measured after rain.

Table 2. *Overview of five XSs at Rönne Å in Sweden. Coordinates are in SWEREF99. In which, river width indicates the width of two poles, and effective width (shown in brackets) represents the width of two river banks.*

Cross-sections	*Coordinates of markers easting, northing*		*Survey date*	*Average depth (m)*	*River (effective) width (m)*	*Remarks*
	Left streambank	*Right streambank*				
XS1	377178.7262, 6227686.785	377202.9943, 6227709.81	29/08/2023	2.8	33.4 (12.9)	First 5-6 m from each bank very densely vegetated
XS2	381436.6493, 6222655.516	381449.8463, 6222666.31	30/08/2023	0.7	16.0 (15.4)	Flow much faster than other XS. Very rocky, with some vegetation. Only wadable XS
XS3	381204.028, 6222774.967	381207.04, 6222800.617	30/08/2023	1.7	25.8 (8.8)	Densely vegetated first 10 m from right bank
XS5	379629.036, 6226245.33	379618.483, 6226271.15	31/08/2023	2.5	27.8 (14.1)	Densely vegetated on right bank
XS6	379400.035, 6226227.146	379393.676, 6226246.231	31/08/2023	1.7	20.1 (12.9)	Densely vegetated on right bank

4 Results

4.1 PIV and STIV results

In Figure 7, brown points indicate the positions of PIV results in SWEREF99 coordinates. Figure 7b shows an absence of PIV points in the middle area of the PIV coverage. A possible reason is the presence of sunlight on top of ripples that are caused by stones, the PIV technique inaccurately assesses this glint as a pattern to track, but since this glint remains in place, the determined velocity becomes too low and is filtered out as an outlier. In Figures 7c and 7d, the presence of vegetation and absence of seeding causes lack of PIV points close to the river banks. In particular, the lower left part of Figure 7d includes an area without PIV results, mainly because a low-altitude Matrice 300 drone disturbed the flow field during the PIV video acquisition. These blank areas can cause increased uncertainty of the footprint-averaged PIV result.

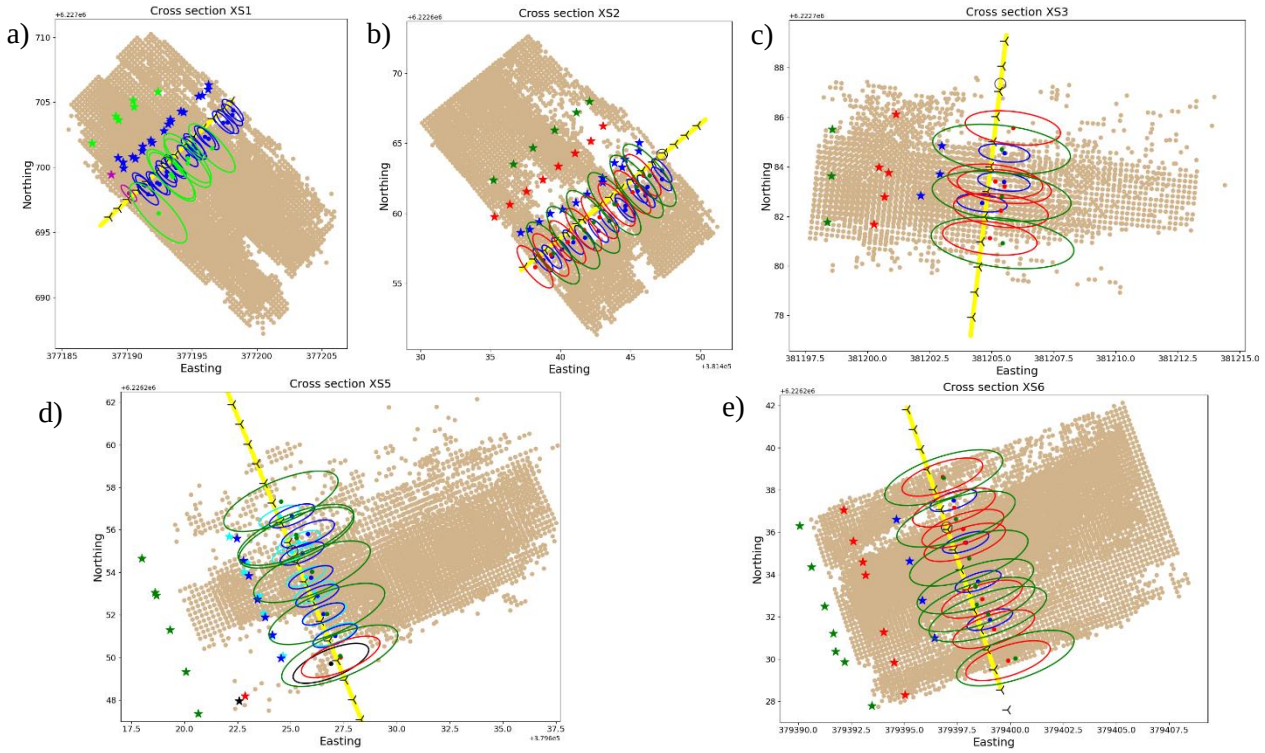

Figure 7. Shows the locations of drone waypoints and footprints with different fly altitudes in SWEREF99 coordinates. In which, stars represent the locations of waypoints, and ellipses indicate the footprint area of Doppler radar combined with drone. Different colors denote the drone with different fly altitudes, details can be found in Figure 6. In addition, yellow lines represent the tagline of each cross-section, and the black circles are the locations of the tagline zero-point. Black left triangles along the tagline present the measuring positions by using OTT MF Pro. Finally, brown points in the area of coordinates are generated by using the PIV approach. Noted that aqua (2.1 m) and black (4.1 m) colors in Figure 7d represent the measured waypoints and footprints before rain.

In Figure 9, grey circles show the STIV measured velocity along the taglines. The average and max surface velocities in five XSs can be found in Table 1. An interesting finding is that the STIV results are not affected by the low-altitude drone in XS5 shown in Figure 9d, while PIV results are smaller than normal velocities due to the drone propwash. The main reason is that the area influenced by propwash covers only a small fraction of the STIV search lines.

4.2 Doppler radar results and Footprint analysis

4.2.1 Doppler radar results

As mentioned in section 2.4, a Gaussian two peak model was used for processing Doppler raw data for XS1, XS3, XS5, and XS6, while a Gaussian one peak model was applied for XS2.

Before fitting to the Gaussian model, we determine maximum velocity (V_{max}), the minimum velocity (V_{min}) from the Doppler spectrum. Moreover, velocities with magnitude less than mask velocity (V_{mask}) are filtered out because the Doppler radar does not produce reliable results for low velocities. We chose a relatively high $V_{mask} = 20$ cm/s in this study, because velocities of interest are much higher than that in all XSs. V_{max} And V_{min} are adjusted for each XS, the selected parameters can be found in Tables A1, A2, A3, A4, and A5.

In XS1, three different flight altitudes, 1.5 m, 2.1 m, and 5.1 m, were executed by UAS-Doppler radar. Meanwhile, flight altitudes of 2.1 m, 4.1 m, and 6.1 m were chosen for the other XSs. The exact locations of all waypoints can be found in Figure 6 (circles) and Figure 7 (stars). Figure 8 shows selected waypoint results for various flight heights for the five XSs, where blue lines are derived from the Gaussian two peak model for all XSs. Black points show the normalized average amplitudes of reselected traces. Symbols $mu1$ and $mu2$ indicate the fitted river surface velocity and the total velocity, using the function of 'scipy.optimize.curve_fit' between modelled results and observed values. In Figures 8b-1, 8b-2, and 8b-3, we plotted both two peak model fitted results (blue lines) and one peak model fitted results (orange lines) for XS2, simultaneously. A comparison of the results indicates that, for XS2, the Gaussian one peak model should be selected due to better correspondence with the PIV and OTT MF Pro results. The Doppler radar velocities at all waypoints are described in Tables A1, A2, A3, A4, and A5, for a total of five different fligh altitudes (1.5 m, 2.1 m, 4.1 m, 5.1 m, and 6.1 m) of UAS-equipped Doppler radar. Results indicate no one altitude seems to work better than the others when comparing Doppler results with PIV and OTT MF Pro results.

4.2.2 Footprint analysis and Doppler-PIV-OTT MF Pro comparisons at waypoints

After determining the Doppler radar location and flight altitude at each waypoint, we can calculate and locate the footprint area according to section 2.3. By analyzing the footprint results, some unrealistic Doppler velocity estimations (e.g. vegetation appears in the footprint area) can be explained. In Figure 7, ellipses with different colors show the footprint areas under different flight altitudes. In combination with PIV results, by computing the histogram and average PIV value within the corresponding footprint, we can compare the mean PIV result to the flow velocity derived from Doppler (Figure 8).

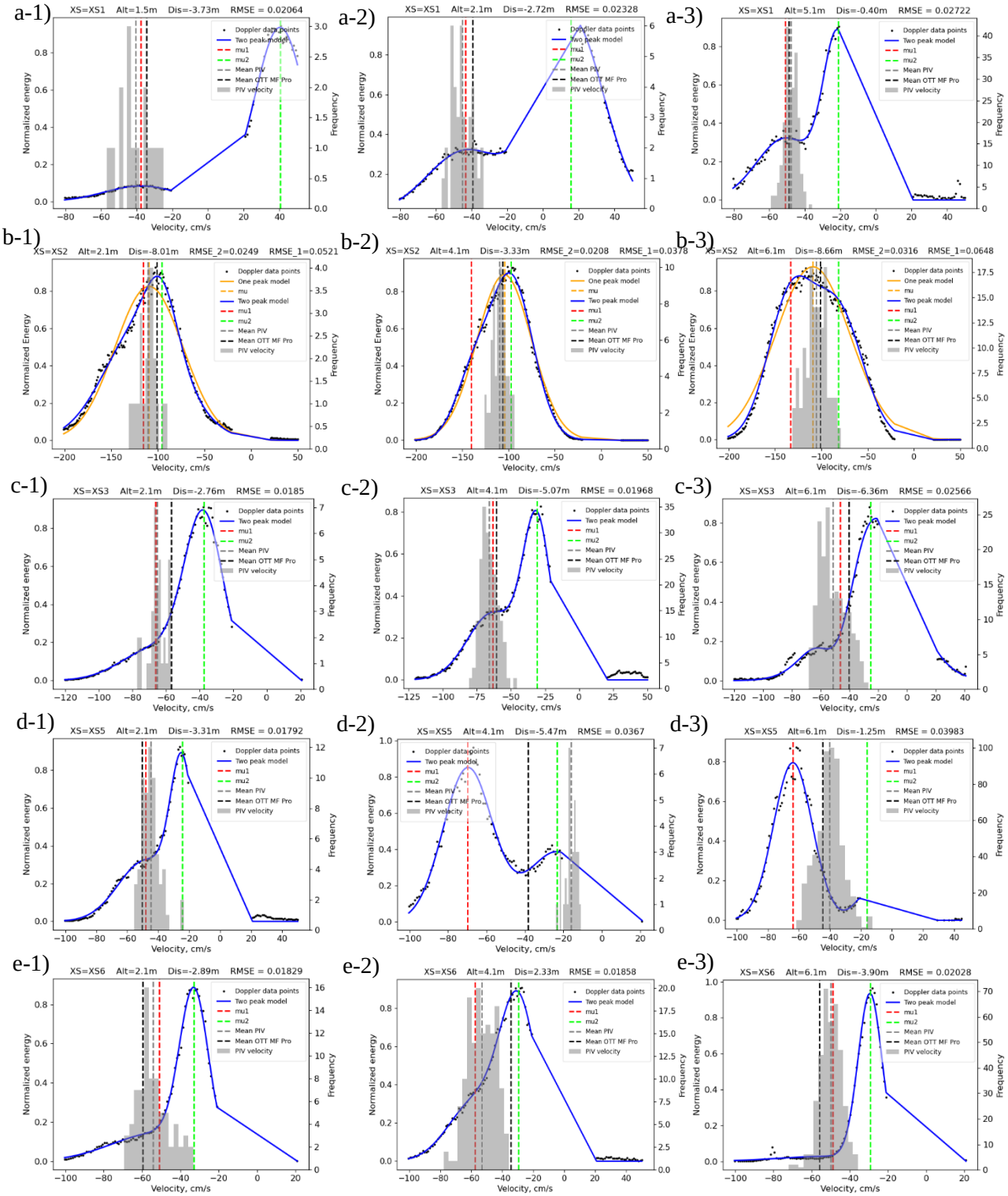

Figure 8. Shows comparisons of mean OTT MF Pro, the histogram of PIV estimated velocities in the footprint, mean PIV, Doppler velocity ($mu1$) by using a Gaussian two peak model , and a Gaussian one peak model (mu) (only shown for XS2). Here negative value means along the river flow direction. Note that $mu2$ represents the total velocity derived from the Gaussian two peak model, which is composed of

481 $mu1$ and the drone-inducted propwash velocity. The mean OTT MF Pro means an average value of two
482 in-situ observed results closest to the waypoint along the tagline.

483 In Figure 8, grey bar charts represent the PIV velocity histogram within the footprint at
484 each waypoint, the bar height shows the frequency of occurrence of velocities in the same range,
485 and the vertical dashed grey line indicates the mean PIV velocity within each footprint. Black
486 vertical dashed lines show the mean OTT MF Pro result, which are calculated by using two in-situ
487 observed results closest to the waypoint location along the tagline. In XS1, XS3, and XS6, we find
488 that Doppler, mean PIV, and mean OTT MF Pro results match well for most waypoints except the
489 waypoint in Figure 8e-2, with differences less than 10 cm/s between three different results. Figure
490 8e-2 shows a much different mean OTT MF Pro value compared to Doppler and mean PIV, the
491 possible reason is caused by unevenly distributed vegetation. In XS2, the Gaussian two peak
492 model fitted results (4.1m: $mu1$= -140.21 cm/s; 6.1m: $mu1$= -133.41 cm/s) are much different
493 from the mean PIV values (4.1m: $MPIV$= -109.61 cm/s; 6.1m: $MPIV$= -105.74 cm/s) under flying
494 altitudes of 4.1 m and 6.1 m, although the solved dashed red line ($mu1$= -115.58 cm/s; $MPIV$= -
495 110.54 cm/s) is acceptable under flight of 2.1 m (Figure 8b-1). To contrast that, the Gaussian one
496 peak model fitted results (2.1m: mu= -109.11 cm/s; 4.1m: mu= -104.41 cm/s; 6.1m: mu= -108.70
497 cm/s) match the mean PIV better for all flight altitudes. Compared with the mean OTT MF Pro
498 results, both Doppler velocity (mu) and mean PIV match well. In XS5, compared with the mean
499 OTT MF Pro results, Figure 8d-1 shows a good match for both the mean PIV and the Doppler
500 radar velocity, while the other two waypoints under flying altitudes of 4.1 m and 6.1 m display
501 inconsistent results. However, we have found a better consistency between the mean PIV and the
502 mean OTT MF Pro in Figure 8d-3. There are two reasons for the low performance at XS5: 1) there
503 is a propwash effect of the low-altitude drone hovering close to XS coordinate -5.5 m during the
504 PIV measurements; 2) the Doppler radar waypoint measurement in Figure 8d-1 was implemented
505 before heavy rain, while the other waypoints Doppler, PIV, and OTT MF Pro measurements were
506 measured after the rain. Figure 8d-2 shows that the mean PIV is close to the total velocity ($mu2$)
507 derived from the Doppler radar, which verifies the propwash effect. In Figure 8d-3, the Doppler
508 radar velocity ($mu1$) is smaller (the absolute value is larger) than the mean PIV and the mean OTT
509 MF Pro result. One possible reason is that the Doppler radar measurement was taken at higher
510 river flow velocity after a significant rainfall event, and that the Doppler radar may be more
511 susceptible to being disturbed by the intermittent small raindrops after the heavy rain than the PIV

and the OTT MF Pro measurements. Combined analysis of Doppler results and PIV results within the Doppler footprint area for all waypoints in the five XSs can be found in Appendix A.

4.3 Comparisons of PIV, STIV, Doppler, and OTT MF Pro

To compare remote sensing results with in-situ point measurement results, we listed PIV results within a max distance of 2.75 m from the tagline (red points), mean PIV values within each footprint (plus symbols), STIV results (grey circles), the Doppler radar velocity (triangles), and

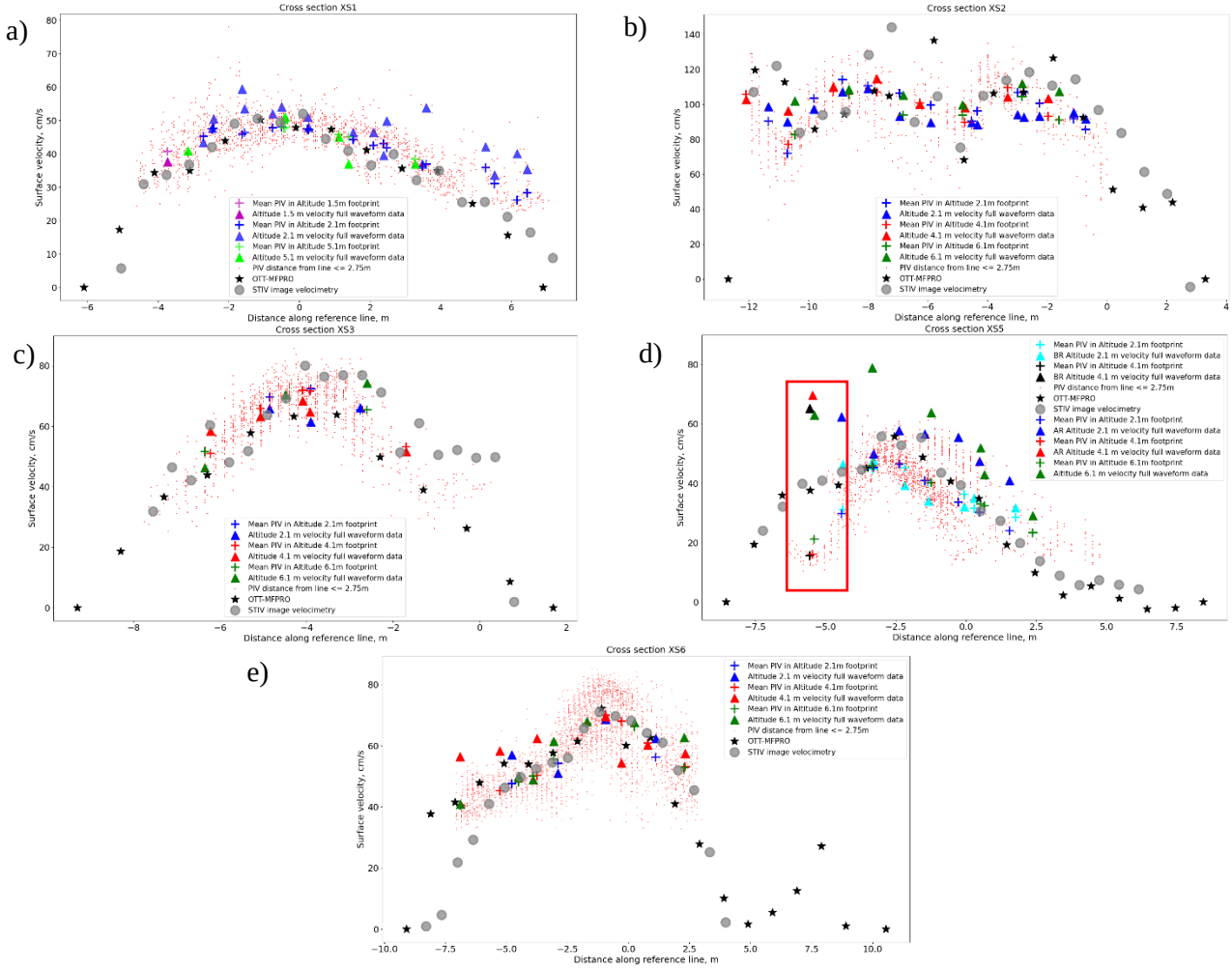

Figure 9. Comparisons of OTT MFPRO results (black stars), STIV image velocities (grey circles), velocities derived from Doppler radar full waveform data (triangle), PIV values by combining u and v component with distance from the tagline <=2.75m (red points), and average PIV values in each elliptical footprint area (plus). Note that in Figure 9d, the red rectangle near -5.5 m shows a larger difference comparing Doppler radar results and PIV values, the main reason is the other drone's propwash effect during the PIV measuring process (see Figure 6d). A positive value means along the river flow direction.

the OTT MF PRO results (black stars) in Figure 9. In addition, a quantitative comparison between OTT MF PRO results and the other three non-invasive measurement techniques is shown in Table 3.

Figure 9a shows better consistency of all results from the different techniques except for some waypoints measured by Doppler radar close to the right bank with a cross-section coordinate larger than 4 m. A main reason for the inconsistency is lower flow velocities under 30 cm/s resulting in a low roughness of river surface, and consequently insufficient signal-to-noise ratio in the Doppler spectra. In Figure 9b, both mean PIV and Doppler radar velocities are lower than OTT MF Pro results close to the left and right banks (approximate distance 2 m from banks), which are affected by vegetation growing on the shallow river bottom. In the middle part of XS2, although there are deviations between Doppler velocities, mean PIV, and OTT MF Pro results at some waypoints because of the fast and highly turbulent flow, Doppler velocities and mean PIV match well overall. In Figure 9c, OTT MF Pro and STIV results exhibit many differences close to the right bank because of the dense vegetation. Although mean PIV and Doppler radar velocities are larger than OTT MF Pro results, both values match well. XS5 is a special case because of drone propwash and heavy rain effects. The red rectangle in Figure 9d indicates the affected area by the drone propwash during PIV measurements, where we can find that Doppler velocity is the highest, the mean PIV results are lowest, and STIV results are matching well with OTT MF Pro. In addition, the Doppler velocities measured after rain are higher than the Doppler velocities before rain except in the propwash-affected area, and the Doppler velocities (after rain) are larger than the mean PIV, STIV, and OTT MF Pro results. The probable reason is increased velocity (increased flow) because of the heavy rain during the Doppler measurements, after that the flow remained constant during the measurements of PIV and OTT MF Pro. A second possible reason is the velocity derived from Doppler is overestimated because of the impact of falling raindrops in the radar footprint. In Figure 9e, differences between STIV and OTT MF Pro are found close to the left bank, probably due to the influence of vegetation. Meanwhile, differences between mean PIV and Doppler velocities at some waypoints close to the left bank are caused by the light rain.

Table 3 shows comparisons between OTT MF Pro results and the other three remote sensing results by computing Root Mean Squared Error (RMSE), Mean Absolute Error (MAE), and Mean Biased Error (MBE). From Table 3, we can find: 1) for XS1, XS3, and XS6, the Doppler radar RMSE, the mean PIV RMSE, and the STIV RMSE are under 11.26 cm/s, 7.62 cm/s, and

13.78 cm/s, respectively. Results indicate that the three remote sensing results and OTT MF Pro observed results match well; 2) in XS2, the Doppler velocity RMSE, the mean PIV RMSE, and the STIV RMSE are 20.07 cm/s, 21.72 cm/s, and 18.48 cm/s, which are approximately equal to or smaller than 20% of the mean velocity (mean velocity is 105 cm/s from XS coordinate -11.8 m to -0.8 m). In addition, the mean PIV result is not better than the Doppler velocity, the possible reason is fluctuating surface velocities are disturbed by some stones located in the shallow river; 3) for XS5, a large Doppler velocity RMSE value of 19.49 cm/s is caused by heavy rain and vegetation. The mean PIV RMSE with 10.54 cm/s is susceptible to the drone propwash and vegetation. However, the drone propwash cannot affect the STIV results with 3.92 cm/s RMSE value because of the search lines with a length of 7.0 m; 4) the Doppler radar generally overestimates surface velocities by using the Gaussian two peak model, as is apparent by the MBE which are all positive except for XS2.

Table 3. *Shows RMSE, MAE, and MBE between OTT MF Pro results and other three measured approaches including Doppler velocity (Doppler), mean PIV (PIV), and Hydro-STIV (STIV) results. In each cross-section, we combined all fly altitudes waypoints Doppler results together. In addition, the other three measured results were linear interpolated based on OTT MF Pro measured locations, afterwards compared them to OTT MF Pro results.*

Cross-sections	*Measured approaches*	*RMSE (cm/s)*	*MAE (cm/s)*	*MBE (cm/s)*
XS1	Doppler	11.26	8.89	8.62
	PIV	6.02	4.67	3.87
	STIV	2.76	2.26	0.49
XS2	Doppler	20.07	15.78	-5.51
	PIV	21.72	16.67	-6.60
	STIV	18.48	14.49	3.55
XS3	Doppler	9.00	7.12	7.12
	PIV	7.62	7.23	7.23
	STIV	13.78	12.61	10.83
XS5	Doppler	19.49	17.26	17.26
	PIV	10.54	8.91	-4.67
	STIV	3.92	3.53	2.33
XS6	Doppler	8.75	5.74	3.59
	PIV	6.01	4.86	-0.52
	STIV	10.07	7.40	-2.89

4.4 A Comparison between Doppler velocity and total velocity

We integrated Doppler results from all waypoints (including Doppler velocity and total velocity) based on the Gaussian two peak model of all XSs except XS2 into one dataset. The

purpose was to find a relation between two peak values and the drone-induced propwash velocity. However, some waypoints with large difference between Doppler velocity and mean PIV or much smaller total velocities were discarded (details can be found in Table 4). Doppler velocity and total velocity based on the reselected waypoints are plotted in Figure 10. The straight-line fitting was applied under different flight altitudes, and we can obtain four lines with various slopes and intercepts. We interpret the intercepts as the drone-induced velocity and find that they are (-48.08 $\pm$ 16.55) cm/s, (-17.11 $\pm$ 32.04) cm/s, (-6.68$\pm$ 11.16) cm/s, and (-37.05$\pm$9.62) cm/s under the flight altitudes 2.1 m, 4.1 m, a combination between 5.1 m and 6.1 m, and all flight altitudes, respectively. These drone-induced propwash velocities seem to be reasonable because the velocity estimates and flight altitudes are negatively related.

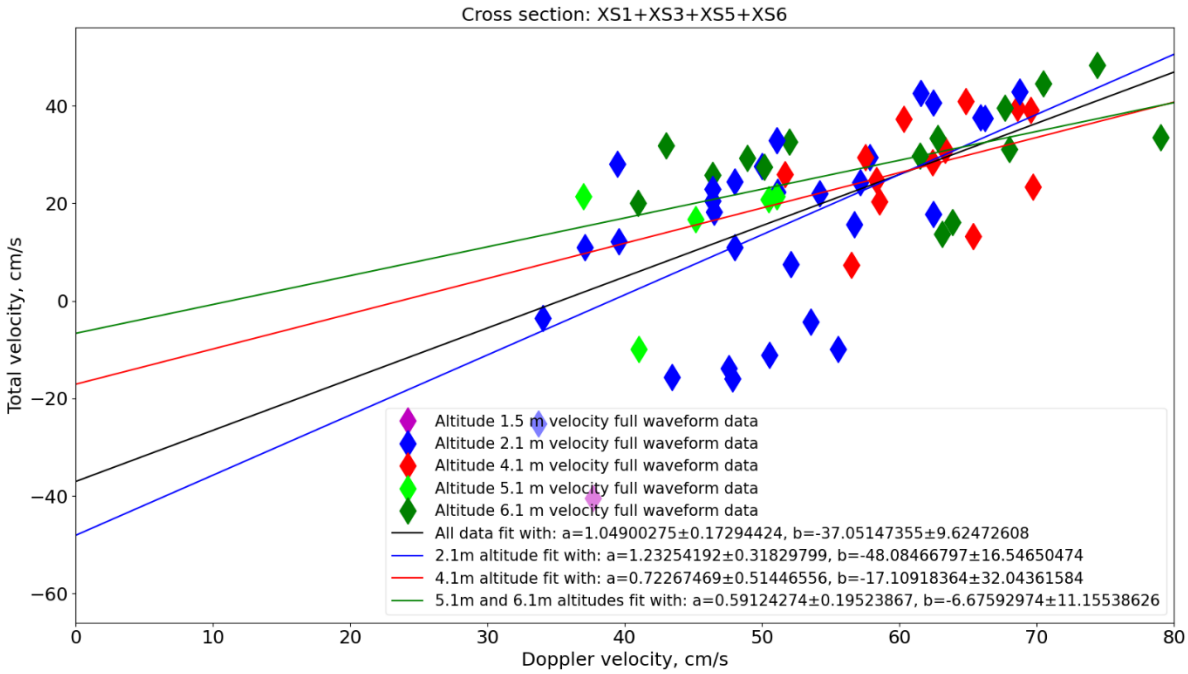

Figure 10. Shows the relation between Doppler velocities and total velocities, in which both are derived from Doppler radar full waveform data by using a Gaussian two peak model. Considering waypoints in XS1 with 5.1 m altitude, the average actual altitude is 5.84 m, therefore we combine 5.1 m altitude with 6.1 m together. From the results of different fly altitudes with 2.1 m, 4.1 m, and a combination of 5.1 m and 6.1 m, we can obtain the drone-inducted propwash velocities become smaller as flight altitude increases. Note that, a positive value means along the river flow, the propwash velocity caused by the drone is always against the river flow. In addition, to fit these straight lines in Figure 10, we discard some waypoints, which are not fit well with PIV results or are too small for total velocities.

Table 4. *Shows some discarded waypoints in Figure 10, in which we can find a larger difference between Doppler velocities and mean PIV values, or much smaller total velocities. A positive means the river flow direction.*

Cross-sections	*Altitudes (m)*	*Waypoints (m)*	*Doppler velocity (cm/s)*	*Total velocity (cm/s)*	*Mean PIV (cm/s)*
XS1	2.1	-1.62	59.48	-6.49	45.90
		2.48	49.89	17.32	41.80
		3.59	53.83	-11.93	36.92
		5.27	42.19	-29.51	35.87
		6.17	40.14	-27.11	26.23
		6.45	35.43	-31.06	28.29
	5.1	1.39	37.01	-28.40	45.14
XS5	2.1	-0.06*	32.13	-31.51	36.32
		0.29*	35.15	-26.96	31.54
		1.55	40.91	-27.86	24.02
		1.76*	31.85	-35.55	28.55
	6.1	2.38	29.20	-26.28	23.33
XS6	4.1	-0.29	54.42	38.92	68.02

* *means these waypoints in XS5 were measured before a heavy rain.*

5 Discussion

OTT MF Pro is still the most reliable velocimetry method in terms of repeatability of results and gives accurate point measurements. Small errors in positioning may occur when having to manually read and note down tagline distance. In addition, because the OTT MF Pro cannot measure exactly at the surface level but needs to be fully submerged, the result does not represent the true surface velocity and does not consider environmental effects, for instance from strong winds.

Furthermore, to make the PIV method fully contactless, seeding operations need to be automatized in the locations where seeding is required. Seeding could be ideally performed by a secondary UAS platform that could release seeding along a diagonal direction relative to the shore to ensure a uniform seeding at the XS where velocity is measured. In general, PIV results contain the highest spatial resolution at the pixel level. In addition, PIV can measure all directions by using parallel and perpendicular river flow direction vector values. However, the necessary ground control points (GCPs) and mask boundaries in the frame must be placed by operators. Furthermore, it is very important to keep the camera stable, especially when the camera is placed on a drone. And the method has strict requirements on survey conditions, such as daylights, winds, vegetation, seeding, and appropriate river width. From the PIV points' distribution in Figure 9, PIV did give results within an acceptable range.

STIV is recognized as a promising technique in real-time monitoring of river flow. Compared to the conventional STIV with manual parameter adjustment (Fujita et al., 2019), we applied the newly released Hydro-STIV with a deep learning-based convolutional neural network (CNN) algorithm to improve the robustness of pattern gradient detection and fully automate the process without manual parameter adjustment (Fujita et al., 2020; Islam et al., 2022). A combination of Figure 9 and Table 3 suggests that current STIV algorithms can provide better surface velocity estimation when excluding some locations close to vegetation. Considering that STIV is based on videos from a UAS-borne camera, similar limitations apply as for PIV; i.e. seeding, daylight, and river width. In comparison, STIV can still work well under deteriorated light conditions. Compared to PIV results with vector points distributed in a 2D domain, STIV results are only distributed along the search line.

Compared to PIV and STIV, UAS-equipped Doppler radar is more suitable for large and wide rivers without requiring seeding and daylight. The Doppler radar requires a minimum roughness of the river surface, this did not seem to be a problem in most areas of this survey but may be a problem in low flow cross-sections affected by vegetation close to banks (i.e., surface velocity < 30 cm/s). Postprocessing of raw radar data based on a Gaussian one peak (or two peak) model can be fully automatized, which can allow real-time velocity determination. However, the velocity measured by the Doppler radar is only in its line of sight, it cannot measure velocities in other directions.

6 Conclusions

We report on measuring river surface velocity using a UAS-drone Doppler radar technique. The applicability of radar velocimetry was evaluated through a series of cross-section experiments carried out within a 10 km stretch of Rönne Å in Sweden. Five different flight altitudes were performed: 1.5 m, 2.1 m, 4.1 m, 5.1m, and 6.1 m above the water surface. The river surface velocity profiles derived from Doppler radar were compared with data obtained from a conventional electromagnetic velocity sensor technique (OTT MF Pro), as well as PIV and STIV.

The approach of using a Gaussian model to fit the average full waveform raw Doppler spectra was proposed for the first time. Based upon this approach, we can find the Doppler velocity by referring to the Gaussian one peak value when the river flow surface velocity is faster than 80 cm/s. When the river flow velocities are between 30 cm/s and 80 cm/s, the left peak value from

649 the Gaussian two peak model represents the river surface velocity, while the right peak value is
650 considered as the total velocity, which is the sum of the flow velocity and the drone propwash
651 velocity. Although Doppler velocity results indicate no one altitude seems to work better than the
652 other flight altitudes, we can find a weak negative correlation between drone-induced propwash
653 velocities and flight altitudes.

654 To verify the Doppler velocity, the footprint analysis combined with PIV results was
655 implemented. Overall, errors between Doppler velocity and mean PIV velocity within the footprint
656 are under 20% apart from some special waypoints, such as those affected by vegetation, rain, and
657 propwash interference. The footprint analysis combining PIV results illustrates the Doppler
658 velocities are reasonable. In addition, STIV and electromagnetic velocity sensor data (OTT MF
659 Pro) results were shown for five XSs, where we find that Doppler velocity, PIV, and STIV results
660 remain consistent with OTT MF Pro results for XS1, XS3, and XS6. For XS2 (surface velocity >
661 80 cm/s), RMSE values between three contactless approaches results and in-situ results are
662 acceptable, i.e. approximately equal to or less than 20% of the average flow velocity. For XS5, the
663 Doppler velocity measured after a heavy rain is higher than both the Doppler velocity measured
664 before the rain and the other three different measurement results (PIV, STIV, and OTT MF Pro).
665 Compared results in XS5 indicate that Doppler radar velocities are more sensitive to rainfall.

666 In summary, combining PIV and STIV based on UAS-borne RGB imagery with the OTT
667 MF Pro results verifies the reliability of Doppler velocity; therefore, we conclude that UAS-borne
668 Doppler radar is an effective technique to measure the river surface flow velocity.

669 **APPENDIX A**

670 **Detailed comparisons between Doppler velocity and mean PIV velocity**

671 To plot Figure 10, some waypoints with a large difference between Doppler velocity and
672 mean PIV or much smaller total velocities were discarded. Details of discarded waypoints are
673 shown in Table 4 and Tables 1A, 4A, and 5A (marked as $^{\#}$). In XS1, these discarded waypoints
674 contain a large difference between Doppler velocity and mean PIV with the absolute error values
675 (*(Dopv-MPIV)/ MPIV)* from 17.63% to 53.03%. In XS5, these discarded waypoints contain very
676 small total velocities (positive and negative represent large and small) from -35.55 cm/s to -26.28
677 cm/s, which means the calculated propwash velocities are unreasonable from -68.77 cm/s to -55.48

cm/s. In XS6, only one waypoint with a larger error value (-19.99%) with a cross-section coordinate -0.29 m waypoint was discarded, while reserving other waypoints with larger errors close to the left bank, the possible reason is smaller mean PIV values caused by vegetation, and the light rain only amplifies the Doppler velocity without changing the propwash velocity.

A Doppler radar velocity is an average value within the ellipse footprint; therefore, we compare the Doppler velocity to the mean PIV values located in the footprint. In Table 1A (XS1), we have found that the absolute values of errors ((*Dopv*-*MPIV*)/*MPIV*) are under 16% when some waypoints (the same waypoints as in Table 4) are excluded, these values verify a good consistency between Doppler velocity and mean PIV within the footprint. In Table 2A (XS2), the absolute errors in most waypoints are under 18% except for three waypoints close to -10.6 m, these three waypoints are affected by vegetation on the shallow river bottom. The absolute errors of all waypoints from XS3, which are shown in Table 3A, are under 15%. A good consistency between the Doppler velocity and the mean PIV values is shown. For XS5 in Table 4A, results seem to be more complicated than other XSs due to a heavy rain and the other drone propwash effects. Some findings are followings: 1) Doppler velocities measured before rain match the mean PIV results better than Doppler velocities measured after rain; 2) Apart from five waypoints as listed in Table 4, the other three waypoints close to -5.5 m are larger errors due to the lower distorted PIV values disturbed by propwash; 3) Doppler results with flight altitudes 2.1 m and 6.1 m under after rain show large errors; meanwhile, the PIV measurements of XS5 are also after rain. Generally, there should be a better consistency between Doppler velocities and mean PIV results under the same condition: after rain. However, the compared results are opposite to the expectations. The possible two reasons are described in section 4.3. For XS6 in Table 5A, there are five waypoints with absolute errors larger than 20% (only one waypoint is in Table 4 due to this waypoint being located middle part of the tagline), these large errors are possibly caused by the light rain after heavy rainfall and vegetation close to banks.

703 **Table 1A.** *Shows all waypoints in XS1. In which 'Vmax/Vmin' parameters are used as boundaries of observed data velocities, 'Tracethreshold' is*
704 *used to reselect traces. 'RMSE' values are computed between* $Mdata_{new}$ *and fitted data with (or without)* $sigma$*. The fitted 'Doppler velocity',*
705 *'Total velocity', and mean PIV in footprint are also listed for further comparison.* [#] *shows these waypoints are discarded corresponding to waypoints*
706 *in Table 4. A positive means the river flow direction.*

Cross-sections	*Altitudes (m)*	*Waypoints (m)*	*Vmax/Vmin (cm/s)*	*Tracethr-eshold*	*Using sigma*	*RMSE*	*Doppler velocity (cm/s)*	*Total velocity(cm/s)*	*Mean PIV (cm/s)*	*(Dopv-MPIV)/ MPIV*
XS1	1.5	-3.73	50/-80	0.0632	no	0.02064	37.70	-40.39	40.79	-7.57%
	2.1	-2.72	50/-80	0.1127	yes	0.02328	43.46	-15.57	45.20	-3.84%
		-2.46	50/-80	0.3197	no	0.02230	47.84	-15.89	47.50	0.72%
		-2.42	50/-80	0.1800	yes	0.06703	50.55	-11.09	47.73	5.91%
		-1.62[#]	50/-80	0.2350	yes	0.02602	59.48	-6.49	45.90	29.59%
		-1.56	50/-80	0.1000	no	0.02733	53.54	-4.27	46.45	15.27%
		-0.76	50/-80	0.1754	yes	0.02461	52.07	7.56	47.79	8.96%
		-0.51	50/-80	0.1000	no	0.04924	54.18	22.07	48.13	12.57%
		0.23	50/-80	0.1161	yes	0.03545	51.11	22.28	47.52	7.56%
		0.26	50/-80	0.1000	no	0.03886	48.02	10.93	47.28	1.56%
		1.51	50/-80	0.1091	yes	0.02890	46.40	20.55	44.33	4.66%
		2.10	50/-80	0.0428	yes	0.03440	46.53	18.26	42.61	9.20%
		2.38	50/-80	0.2199	no	0.02577	39.59	12.23	43.15	-8.24%
		2.48[#]	50/-80	0.1600	yes	0.03502	49.89	17.32	41.80	19.35%
		3.48	50/-80	0.1565	yes	0.03349	37.09	10.99	36.27	2.27%
		3.59[#]	50/-80	0.1322	no	0.03583	53.83	-11.93	36.92	45.81%
		5.27[#]	50/-80	0.0623	no	0.02708	42.19	-29.51	35.87	17.63%
		5.53	50/-80	0.1121	no	0.02221	33.73	-25.22	31.07	8.55%
		6.17[#]	50/-80	0.2555	yes	0.03839	40.14	-27.11	26.23	53.03%
		6.45[#]	50/-80	0.0412	yes	0.05264	35.43	-31.06	28.29	25.23%
	5.1	-3.15	30/-70	0.1751	no	0.03629	41.03	-9.96	40.28	1.86%
		-0.45	20/-80	0.1134	no	0.02622	50.51	20.80	47.72	5.84%
		-0.40	50/-80	0.1153	no	0.02722	51.06	21.37	47.95	6.49%
		1.12	40/-90	0.0892	no	0.03446	45.19	16.77	45.81	-1.36%
		1.39[#]	50/-80	0.0727	no	0.03130	37.01	-28.40	45.14	-18.02%
		3.28	50/-80	0.0826	yes	0.01900	37.00	21.33	38.47	-3.81%

707

Table 2A. *Shows all waypoints in XS2. In which 'Vmax/Vmin' parameters are used as boundaries of observed data velocities, 'Tracethreshold' is used to reselect traces. 'RMSE' values are computed between* $Mdata_{new}$ *and fitted data with (or without)* $sigma$*. The fitted 'Doppler velocity', 'Total velocity', and mean PIV in footprint are also listed for further comparison. A positive means the river flow direction.*

Cross-sections	*Altitudes (m)*	*Waypoints (m)*	*Vmax/Vmin (cm/s)*	*Tracethre-shold*	*Using sigma*	*RMSE*	*Doppler velocity (cm/s)*	*Total velocity(cm/s)*	*Mean PIV (cm/s)*	*(Dopv-MPIV)/ MPIV*
XS2	2.1	-11.34	50/-200	0.1164	no	0.02448	98.89	nan	90.44	9.34%
		-10.71	50/-200	0.1162	no	0.01575	90.08	nan	71.87	25.34%
		-9.82	50/-200	0.1162	no	0.02199	97.38	nan	103.58	-5.99%
		-8.87	50/-200	0.1150	no	0.02869	107.36	nan	114.19	-5.98%
		-8.01	50/-200	0.1157	no	0.02492	109.11	nan	110.54	-1.29%
		-6.95	50/-200	0.1162	no	0.02029	93.48	nan	106.43	-12.17%
		-5.91	50/-200	0.1157	no	0.02884	89.68	nan	99.58	-9.94%
		-4.53	50/-200	0.1172	no	0.02454	89.80	nan	90.35	-0.61%
		-4.35	50/-200	0.1162	no	0.02135	88.58	nan	96.30	-8.02%
		-3.00	50/-200	0.1162	no	0.01771	94.19	nan	106.72	-11.74%
		-2.79	50/-200	0.1181	no	0.01825	92.81	nan	106.76	-13.07%
		-2.26	50/-200	0.1150	no	0.01902	93.41	nan	100.72	-7.26%
		-1.11	50/-200	0.1157	no	0.02199	95.42	nan	91.81	3.93%
		-0.72	50/-200	0.1181	no	0.03066	91.75	nan	85.73	7.02%
	4.1	-12.09	50/-200	0.1164	no	0.02871	102.95	nan	105.81	-2.70%
		-10.68	50/-200	0.1172	no	0.04222	96.45	nan	77.11	25.08%
		-9.18	50/-200	0.1162	no	0.03093	110.13	nan	107.53	2.42%
		-7.72	50/-200	0.1145	no	0.03585	114.86	nan	107.18	7.17%
		-6.28	50/-200	0.1162	no	0.03110	100.20	nan	100.78	-0.58%
		-4.76	50/-200	0.1157	no	0.03582	98.16	nan	89.68	9.46%
		-3.33	50/-200	0.1157	no	0.03588	104.41	nan	109.61	-4.74%
		-1.96	50/-200	0.1157	no	0.04243	103.50	nan	93.09	11.18%
	6.1	-10.46	50/-200	0.1164	no	0.03572	102.02	nan	82.60	23.51%
		-8.66	50/-200	0.1162	no	0.06556	108.70	nan	105.74	2.80%
		-6.83	50/-200	0.1164	no	0.03498	105.24	nan	94.06	11.89%
		-4.85	50/-200	0.1162	no	0.03306	99.86	nan	93.81	6.45%
		-2.84	50/-200	0.1164	no	0.04265	111.98	nan	104.58	7.08%
		-1.61	50/-200	0.1114	no	0.04744	107.53	nan	91.19	17.92%

Table 3A. *Shows all waypoints in XS3. In which 'Vmax/Vmin' parameters are used as boundaries of observed data velocities, 'Tracethreshold' is used to reselect traces. 'RMSE' values are computed between* $Mdata_{new}$ *and fitted data with (or without)* $sigma$*. The fitted 'Doppler velocity', 'Total velocity', and mean PIV in footprint are also listed for further comparison. A positive means the river flow direction.*

Cross-sections	*Altitudes (m)*	*Waypoints (m)*	*Vmax/Vmin (cm/s)*	*Tracethre-shold*	*Using sigma*	*RMSE*	*Doppler velocity (cm/s)*	*Total velocity(cm/s)*	*Mean PIV (cm/s)*	*(Dopv-MPIV)/ MPIV*
XS3	2.1	-4.86	30/-100	0.2000	yes	0.08833	65.92	37.52	69.68	-5.40%
		-3.91	30/-100	0.0953	no	0.01732	61.57	42.60	72.38	-14.94%
		-2.76	20/-120	0.1066	no	0.01850	66.22	37.46	65.45	1.18%
	4.1	-6.22	50/-120	0.1907	no	0.02850	58.54	20.34	51.02	14.74%
		-5.07	50/-120	0.1790	no	0.01968	63.33	30.97	65.85	-3.83%
		-4.09	50/-120	0.1159	no	0.02874	68.59	39.60	71.94	-4.66%
		-3.92	50/-120	0.1035	yes	0.02682	64.82	40.90	71.70	-9.60%
		-1.71	50/-108	0.0895	no	0.01676	51.68	25.97	53.29	-3.02%
	6.1	-6.36	40/-120	0.1036	yes	0.05924	46.40	25.76	51.64	-10.15%
		-4.49	40/-120	0.1148	yes	0.05088	70.49	44.49	69.18	1.89%
		-2.60	40/-120	0.1238	yes	0.02714	74.38	48.30	65.50	13.56%

Table 4A. *Shows all waypoints in XS5. In which 'Vmax/Vmin' parameters are used as boundaries of observed data velocities, 'Tracethreshold' is used to reselect traces. 'RMSE' values are computed between* $Mdata_{new}$ *and fitted data with (or without)* $sigma$*. The fitted 'Doppler velocity', 'Total velocity', and mean PIV in footprint are also listed for further comparison.* $^{\#}$ *shows these waypoints are discarded corresponding to waypoints in Table 4. A positive means the river flow direction.*

Cross-sections	*Altitudes (m)*	*Waypoints (m)*	*Vmax/Vmin (cm/s)*	*Tracethre-shold*	*Using sigma*	*RMSE*	*Doppler velocity (cm/s)*	*Total velocity(cm/s)*	*Mean PIV (cm/s)*	*(Dopv-MPIV)/ MPIV*
XS5	2.1	-4.39*	20/-100	0.0900	no	0.02009	46.40	22.85	31.16	48.91%
		-3.31*	50/-100	0.0811	no	0.01792	47.98	24.48	44.81	7.07%
		-2.19*	50/-100	0.1344	no	0.01470	39.47	28.03	45.21	-12.70%
		-1.34*	50/-100	0.1100	no	0.02680	34.03	-3.56	40.36	-15.68%
		-0.06*#	50/-100	0.1333	no	0.02745	32.13	-31.51	36.32	-11.54%
		0.29*#	50/-100	0.1748	no	0.02200	35.15	-26.96	31.54	11.45%
		1.76*#	50/-100	0.1079	yes	0.01961	31.85	-35.55	29.76	7.02%
		-4.44	50/-100	0.0989	yes	0.02029	62.48	17.81	45.39	37.65%
		-3.29	50/-100	0.1136	no	0.03065	49.98	27.56	46.57	7.32%
		-2.38	50/-100	0.0800	no	0.02609	57.87	29.48	40.92	41.42%
		-1.47	50/-100	0.1926	no	0.01756	56.72	15.63	33.73	68.16%
		-0.28	50/-100	0.1100	yes	0.02665	55.54	-9.88	30.23	83.72%
		0.47	50/-100	0.3377	no	0.01827	47.56	-13.77	24.02	98.00%
		1.55#	50/-100	0.1667	no	0.01758	40.91	-27.86	31.16	31.29%
	4.1	-5.57*	50/-100	0.1108	no	0.02265	65.38	13.18	15.59	319.37%
		-5.47	20/-100	0.0965	no	0.03670	69.74	23.33	16.06	334.25%
	6.1	-5.40	50/-100	0.1138	no	0.03887	63.12	13.63	21.15	198.44%
		-3.35	50/-100	0.1121	no	0.02936	79.04	33.48	45.94	72.05%
		-1.25	50/-100	0.0991	no	0.03983	63.89	16.13	40.23	58.81%
		0.65	50/-100	0.0850	no	0.04267	43.00	31.84	32.97	30.42%
		0.52	50/-100	0.1445	no	0.02936	52.00	32.56	32.45	60.25%
		2.38#	50/-100	0.1190	no	0.02696	29.20	-26.28	23.33	25.16%

* *Means these waypoints in XS5 were measured before a heavy rain.*

720 **Table 5A.** *Shows all waypoints in XS6. In which 'Vmax/Vmin' parameters are used as boundaries of observed data velocities, 'Tracethreshold' is*
721 *used to reselect traces. 'RMSE' values are computed between* $Mdata_{new}$ *and fitted data with (or without)* $sigma$*. The fitted 'Doppler velocity',*
722 *'Total velocity', and mean PIV in footprint are also listed for further comparison.* [#] *shows these waypoints are discarded corresponding to waypoints*
723 *in Table 4. A positive means the river flow direction.*
724 .

Cross-sections	*Altitudes (m)*	*Waypoints (m)*	*Vmax/Vmin (cm/s)*	*Tracethre-shold*	*Using sigma*	*RMSE*	*Doppler velocity (cm/s)*	*Total velocity(cm/s)*	*Mean PIV (cm/s)*	*(Dopv-MPIV)/ MPIV*
XS6	2.1	-4.78	50/-100	0.1000	no	0.02200	57.15	24.28	47.55	20.19%
		-2.89	20/-100	0.0930	no	0.01829	51.06	32.95	54.23	-5.85%
		-0.95	50/-100	0.0943	no	0.02269	68.75	42.87	70.12	-1.95%
		1.11	50/-100	0.1168	no	0.02626	62.45	40.60	56.25	11.02%
	4.1	-6.90	50/-100	0.0696	no	0.01230	56.53	7.40	40.63	39.13%
		-5.27	50/-100	0.2832	no	0.01908	58.32	24.70	45.21	29.00%
		-3.74	50/-100	0.0450	no	0.01664	62.40	28.36	50.23	24.23%
		-0.94	50/-100	0.2384	no	0.02343	69.59	39.12	69.93	-0.49%
		-0.29[#]	50/-100	0.0828	no	0.02352	54.42	38.92	68.02	-19.99%
		0.79	50/-100	0.1156	no	0.02134	60.31	37.27	60.94	-1.03%
		2.33	50/-100	0.0994	no	0.01858	57.52	29.46	53.19	8.14%
	6.1	-6.89	50/-100	0.0800	no	0.03623	40.97	20.07	40.47	1.24%
		-4.51	20/-100	0.0700	no	0.02047	50.15	27.50	48.22	4.00%
		-3.90	20/-100	0.0400	no	0.02028	48.95	29.33	50.01	-2.12%
		-3.07	50/-100	0.0735	no	0.01871	61.50	29.66	55.76	10.29%
		-1.71	50/-100	0.1500	no	0.08003	68.00	31.01	67.34	0.98%
		0.24	50/-100	0.1819	no	0.03315	67.68	39.62	66.22	2.20%
		2.28	50/-100	0.1386	no	0.02347	62.78	33.29	52.81	18.88%

725

Acknowledgments

This work was supported by the European Union's Horizon Europe research and innovation programme as part of the UAWOS project (Unmanned Airborne Water Observing System, Grant Agreement No: 101081783).

Open Research

Data sets used in this are available online in the repository archived in https://figshare.com/s/86d39f030f1a9a5d6c97.

References

Alimenti, F., Bonafoni, S., Gallo, E., Palazzi, V., Gatti, R. V., Mezzanotte, P., ... & Moramarco, T. (2020). Noncontact measurement of river surface velocity and discharge estimation with a low-cost Doppler radar sensor. *IEEE Transactions on Geoscience and Remote Sensing*, *58*(7), 5195-5207.

Alsdorf, D. E., Rodríguez, E., & Lettenmaier, D. P. (2007). Measuring surface water from space. *Reviews of Geophysics*, *45*(2).

Bahmanpouri, F., Barbetta, S., Gualtieri, C., Ianniruberto, M., Filizola, N., Termini, D., & Moramarco, T. (2022a). Prediction of river discharges at confluences based on entropy theory and surface-velocity measurements. *Journal of Hydrology*, 606, 127404.

Bahmanpouri, F., Eltner, A., Barbetta, S., Bertalan, L., & Moramarco, T. (2022b). Estimating the Average River Cross-Section Velocity by Observing Only One Surface Velocity Value and Calibrating the Entropic Parameter. *Water Resources Research*, *58*(10), e2021WR031821.

Bandini, F., Lüthi, B., Peña-Haro, S., Borst, C., Liu, J., Karagkiolidou, S., ... & Bauer-Gottwein, P. (2021). A drone-borne method to jointly estimate discharge and Manning's roughness of natural streams. *Water Resources Research*, *57*(2), e2020WR028266.

Bandini, F., Frías, M. C., Liu, J., Simkus, K., Karagkiolidou, S., & Bauer-Gottwein, P. (2022). Challenges with Regard to Unmanned Aerial Systems (UASs) Measurement of River Surface Velocity Using Doppler Radar. *Remote Sensing*, *14*(5), 1277.

Bechle, A. J., & Wu, C. H. (2014). An entropy-based surface velocity method for estuarine discharge measurement. *Water Resources Research, 50*(7), 6106-6128.

Biondi, F., Addabbo, P., Clemente, C., & Orlando, D. (2020). Measurements of surface river doppler velocities with along-track InSAR using a single antenna. *IEEE Journal of Selected Topics in Applied Earth Observations and Remote Sensing*, 13, 987-997.

Chan, Y. T., & Jardine, F. L. (1990). Target localization and tracking from Doppler-shift measurements. *IEEE Journal of Oceanic Engineering, 15*(3), 251-257.

Detert, M., & Weitbrecht, V. (2015). A low-cost airborne velocimetry system: proof of concept. *Journal of Hydraulic Research, 53*(4), 532-539.

De Schoutheete, F. E. R. D. I. N. A. N. D., D'Odeigne, O. C., & Soares-Frazão, S. A. N. D. R. A. (2019, September). *Drone-Driven Surface Velocity Measurements in Natural Rivers*. In Proceedings of the 38th IAHR World Congress, Panama City, Panama (pp. 1-6).

Egg, L., Mueller, M., Pander, J., Knott, J., & Geist, J. (2017). Improving European Silver Eel (Anguilla anguilla) downstream migration by undershot sluice gate management at a small-scale hydropower plant. *Ecological Engineering*, 106, 349-357.

Eker, R., Elvanoglu, N., Ucar, Z., Bilici, E., & Aydın, A. (2022). 3D modelling of a historic windmill: PPK-aided terrestrial photogrammetry vs smartphone app. The International Archives of the Photogrammetry, *Remote Sensing and Spatial Information Sciences*, 43, 787-792.

Fujita, I., Watanabe, H., & Tsubaki, R. (2007). Development of a non-intrusive and efficient flow monitoring technique: The space-time image velocimetry (STIV). *International Journal of River Basin Management, 5*(2), 105-114.

Fujita, I., & Kunita, Y. (2011). Application of aerial LSPIV to the 2002 flood of the Yodo River using a helicopter mounted high density video camera. *Journal of Hydro-environment Research, 5*(4), 323-331.

Fujita, I., Notoya, Y., Tani, K., & Tateguchi, S. (2019). Efficient and accurate estimation of water surface velocity in STIV. *Environmental Fluid Mechanics*, 19, 1363-1378.

778 Fujita, I., Shibano, T., & Tani, K. (2020). Application of masked two-dimensional Fourier spectra
779 for improving the accuracy of STIV-based river surface flow velocity measurements.
780 *Measurement Science and Technology*, *31*(9), 094015.

781 Fulton, J., & Ostrowski, J. (2008). Measuring real-time streamflow using emerging technologies:
782 Radar, hydroacoustics, and the probability concept. *Journal of Hydrology*, *357*(1-2), 1-10.

783 Fulton, J. W., Anderson, I. E., Chiu, C. L., Sommer, W., Adams, J. D., Moramarco, T., ... & Pulli,
784 J. J. (2020). QCam: SUAS-based Doppler radar for measuring river discharge. *Remote*
785 *Sensing*, *12*(20), 3317.

786 Ge, M., Gendt, G., Rothacher, M. A., Shi, C., & Liu, J. (2008). Resolution of GPS carrier-phase
787 ambiguities in precise point positioning (PPP) with daily observations. *Journal of geodesy*, 82,
788 389-399.

789 Hain, R., & Kähler, C. J. (2007). Fundamentals of multiframe particle image velocimetry (PIV).
790 *Experiments in fluids*, 42, 575-587.

791 Islam, M. T., Yoshida, K., Nishiyama, S., Sakai, K., Adachi, S., & Pan, S. (2022). Promises and
792 uncertainties in remotely sensed riverine hydro-environmental attributes: Field testing of novel
793 approaches to unmanned aerial vehicle-borne lidar and imaging velocimetry. *River Research and*
794 *Applications*, *38*(10), 1757-1774.

795 Kempe, C., Jivall, L., Lidberg, M., & Lilje, M. (2016). On the management of reference frames in
796 Sweden. In *Proceedings of the FIG Working Week*.

797 Lacambre, J. B., Barford, T., Oudart, N., Lieffering, P., Morvant, G., & Guyot, B. (2022,
798 September). *Optimizing High Precision RTK/PPK GNSS Algorithms Using Real-World Data*. In
799 Proceedings of the 35th International Technical Meeting of the Satellite Division of The Institute
800 of Navigation (ION GNSS+ 2022) (pp. 1746-1759).

801 Legleiter, C. J., & Kinzel, P. J. (2020). Inferring surface flow velocities in sediment-laden Alaskan
802 rivers from optical image sequences acquired from a helicopter. *Remote Sensing*, *12*(8), 1282.

Lin, Y. S., Chiu, S. F., & Chang, C. H. (2020). A 24 GHz hydrology radar system capable of wide-range surface velocity detection for water resource management applications. *Microwave and Optical Technology Letters*, *62*(11), 3463-3475.

Luce, C. H., Tonina, D., Gariglio, F., & Applebee, R. (2013). Solutions for the diurnally forced advection-diffusion equation to estimate bulk fluid velocity and diffusivity in streambeds from temperature time series. *Water Resources Research*, *49*(1), 488-506.

Mutzner, L., Vermeirssen, E. L., Mangold, S., Maurer, M., Scheidegger, A., Singer, H., ... & Ort, C. (2019). Passive samplers to quantify micropollutants in sewer overflows: Accumulation behaviour and field validation for short pollution events. *Water research*, 160, 350-360.

Plant, W. J., & Keller, W. C. (1990). Evidence of Bragg scattering in microwave Doppler spectra of sea return. *Journal of Geophysical Research: Oceans*, *95*(C9), 16299-16310.

Plant, W. J. (1997). A model for microwave Doppler sea return at high incidence angles: Bragg scattering from bound, tilted waves. *Journal of Geophysical Research: Oceans*, *102*(C9), 21131-21146.

Plant, W. J., Keller, W. C., & Hayes, K. (2005). Measurement of river surface currents with coherent microwave systems. *IEEE Transactions on Geoscience and Remote Sensing*, *43*(6), 1242-1257.

Randklev, C. R., Hart, M. A., Khan, J. M., Tsakiris, E. T., & Robertson, C. R. (2019). Hydraulic requirements of freshwater mussels (Unionidae) and a conceptual framework for how they respond to high flows. *Ecosphere*, *10*(12), e02975.

Shames, I., Bishop, A. N., Smith, M., & Anderson, B. D. (2013). Doppler shift target localization. *IEEE Transactions on Aerospace and Electronic Systems*, *49*(1), 266-276.

Shi, H., Liang, X., Huai, W., & Wang, Y. (2019). Predicting the bulk average velocity of open-channel flow with submerged rigid vegetation. *Journal of Hydrology*, 572, 213-225.

Siegert, M., Jeofry, H., Corr, H., Ross, N., Jordan, T., Ferraccioli, F., ... & Robinson, C. (2017). Synthetic-aperture radar (SAR) processed airborne radio-echo sounding data from the Institute and

Moller ice streams, West Antarctica, 2010-11, Cambridge, Polar Data Centre, Natural Environment Research Council, UK, 16.2 GB.

Strelnikova, D., Paulus, G., Käfer, S., Anders, K. H., Mayr, P., Mader, H., ... & Schneeberger, R. (2020). Drone-based optical measurements of heterogeneous surface velocity fields around fish passages at hydropower dams. *Remote Sensing*, *12*(3), 384.

Taddia, Y., Stecchi, F., & Pellegrinelli, A. (2019). Using DJI Phantom 4 RTK drone for topographic mapping of coastal areas. The International Archives of the Photogrammetry, *Remote Sensing and Spatial Information Sciences*, 42, 625-630.

Tamimi, R., & Toth, C. (2023). Assessing the Viability of PPK Techniques for Accurate Mapping with UAS. The International Archives of the Photogrammetry, *Remote Sensing and Spatial Information Sciences*, 48, 479-488.

Tauro, F., Porfiri, M., & Grimaldi, S. (2014). Orienting the camera and firing lasers to enhance large scale particle image velocimetry for streamflow monitoring. *Water Resources Research, 50*(9), 7470–7483.

Tauro, F., Porfiri, M., & Grimaldi, S. (2016). Surface flow measurements from drones. *Journal of Hydrology,* 540, 240–245.

Tauro, F., Olivieri, G., Petroselli, A., Porfiri, M., & Grimaldi, S. (2016). Flow monitoring with a camera: a case study on a flood event in the Tiber river. *Environmental monitoring and assessment*, 188, 1-11.

Tauro, F., Piscopia, R., & Grimaldi, S. (2017). Streamflow observations from cameras: Large-scale particle image velocimetry or particle tracking velocimetry?. *Water Resources Research, 53*(12), 10374-10394.

Welber, M., Le Coz, J., Laronne, J. B., Zolezzi, G., Zamler, D., Dramais, G., ... & Salvaro, M. (2016). Field assessment of noncontact stream gauging using portable surface velocity radars (SVR). *Water Resources Research, 52*(2), 1108-1126.

Westerweel, J. (1995). *Digital particle image velocimetry: Theory and application*.

Yaseen, Z. M., Sulaiman, S. O., Deo, R. C., & Chau, K. W. (2019). An enhanced extreme learning machine model for river flow forecasting: State-of-the-art, practical applications in water resource engineering area and future research direction. *Journal of Hydrology*, 569, 387-408.

Yurovsky, Y. Y., Kudryavtsev, V. N., Grodsky, S. A., & Chapron, B. (2019). Sea surface Ka-band Doppler measurements: Analysis and model development. *Remote Sensing*, *11*(7), 839.

Zhao, H., Chen, H., Liu, B., Liu, W., Xu, C. Y., Guo, S., & Wang, J. (2021). An improvement of the Space-Time Image Velocimetry combined with a new denoising method for estimating river discharge. *Flow Measurement and Instrumentation*, 77, 101864.

Zoltie, T., & Ho, M. (2018). Viability of a modified GoPro for professional surgical videography. *Journal of Plastic, Reconstructive & Aesthetic Surgery*, *71*(8), 1216-1230.